*remote sensing*

MDPI

*Article*

# Comparative Study of the Atmospheric Gas Composition Detection Capabilities of FY-3D/HIRAS-I and FY-3E/HIRAS-II Based on Information Capacity

**Mengzhen Xie [1,2,3], Mingjian Gu [1,3,4,*], Chunming Zhang [1,2,3], Yong Hu [1,3], Tianhang Yang [1,3], Pengyu Huang [5] and Han Li [1,2,3]**

[1] Key Laboratory of Infrared System Detection and Imaging Technologies, Shanghai Institute of Technical Physics, Chinese Academy of Sciences, Shanghai 200083, China; xiemengzhen@mail.sitp.ac.cn (M.X.); zhangchunming@mail.sitp.ac.cn (C.Z.); huyong@mail.sitp.ac.cn (Y.H.); yangtianhang@mail.sitp.ac.cn (T.Y.); lihan2019@mail.sitp.ac.cn (H.L.)
[2] University of Chinese Academy of Sciences, Beijing 100049, China
[3] Shanghai Institute of Technical Physics, Chinese Academy of Sciences, Shanghai 200083, China
[4] Suzhou Academy, Shanghai Institute of Technical Physics, Chinese Academy of Sciences, Suzhou 215000, China
[5] School of Atmospheric Sciences, Sun Yat-sen University, Zhuhai 519082, China; huangpy29@mail2.sysu.edu.cn
* Correspondence: gumingjian@mail.sitp.ac.cn

**Abstract:** Fengyun-3E (FY-3E)/Hyperspectral Infrared Atmospheric Sounder-II (HIRAS-II) is an extension Fengyun-3D (FY-3D)/HIRAS-I. It is crucial to fully explore and analyze the detection capabilities of these two instruments for atmospheric gas composition. Based on the observed spectral data from the infrared hyperspectral detection instruments FY-3D/HIRAS-I and FY-3E/HIRAS-II, simulated radiance data and Jacobian matrices are obtained using the Rapid Radiative Transfer Model RTTOV (Radiative Transfer for TOVS (TIROS Operational Vertical Sounder)). By perturbing temperature (T), surface temperature ($T_{surf}$), water vapor ($H_2O$), ozone ($O_3$), carbon dioxide ($CO_2$), methane ($CH_4$), carbon monoxide (CO), and nitrous oxide ($N_2O$), the brightness temperature differences before and after the perturbations are calculated to analyze the sensitivity of temperature and various atmospheric gas components. The Improved Optimal Sensitivity Profile (OSP) algorithm is used to select the channels for atmospheric gas retrieval. The observation error covariance and background error covariance matrices are calculated, and then the information capacity is calculated, specifically the degrees of freedom for signal(DFS) and the entropy reduction (ER). Based on this, a comparative analysis is conducted on the information capacity of atmospheric water vapor and ozone components contained in the hyperspectral detection data from HIRAS-I and HIRAS-II instruments, respectively, to explore the retrieval capabilities of the two instruments for atmospheric gas components. We selected clear-sky data from the African oceanic region and the Chinese Yangtze River Delta terrestrial region for quantitative analysis of the information capacity of HIRAS-I and HIRAS-II. The results show that FY-3D/HIRAS-I and FY-3E/HIRAS-II exhibit different sensitivities to atmospheric gas components. In different experimental regions, temperature and water vapor show the most dramatic sensitivity changes, followed by ozone, methane, and nitrous oxide, while carbon monoxide and carbon dioxide exhibit the lowest variability. Regarding channel selection, HIRAS-II identifies more gas channels compared to HIRAS-I. The experiments concluded that HIRAS-II has a significantly higher information capacity than HIRAS-I, and the information capacity of atmospheric gas components varies across different experimental regions. Water vapor and ozone exhibit the highest information capacity, followed by nitrous oxide and methane, while carbon monoxide and carbon dioxide demonstrate the lowest capacity. The $H_2O$ ER (DFS) contained in FY-3E/HIRAS-II is 1.51 (0.35) higher than that in FY-3D/HIRAS-I, the $O_3$ ER (DFS) in FY-3E/HIRAS-II is 1.51 (0.36) higher than that in FY-3D/HIRAS-I, while the $N_2O$ ER (DFS) in FY-3E/HIRAS-II is 0.17 (0.19) higher and the $CH_4$ ER (DFS) is 0.07 (0.04) higher than that in FY-3D/HIRAS-I.

**Keywords:** HIRAS-I; HIRAS-II; atmospheric gas composition; gas channels; signal degrees of freedom; entropy reduction; information capacity



**Citation:** Xie, M.; Gu, M.; Zhang, C.; Hu, Y.; Yang, T.; Huang, P.; Li, H. Comparative Study of the Atmospheric Gas Composition Detection Capabilities of FY-3D/HIRAS-I and FY-3E/HIRAS-II Based on Information Capacity. *Remote Sens.* **2023**, *15*, 4096. https://doi.org/10.3390/rs15164096

Academic Editors: Filomena Romano and Elisabetta Ricciardelli

Received: 17 July 2023
Revised: 15 August 2023
Accepted: 18 August 2023
Published: 20 August 2023

## 1. Introduction

In order to improve the accuracy of numerical weather prediction, atmospheric detection has become the main driving force for the development of meteorological satellites in various countries. Meteorological satellites, with their high observation frequency and wide imaging range, have become an indispensable part of the comprehensive observation system. By continuously improving the spectral resolution of infrared detection instruments, meteorological satellites obtain narrower atmospheric weighting functions, thereby improving the vertical resolution of satellite atmospheric detection. They can clearly distinguish the radiation impact of water vapor, ozone, and other trace gases [1]. The operation of hyperspectral detection instruments provides a large amount of observational data on the Earth's atmosphere. Observational data from hyperspectral atmospheric detection instruments have been widely used in global and regional numerical forecast models and have achieved significant positive effects [2]. The reason why the accuracy of atmospheric gas composition parameters derived from satellite remote sensing data varies is because different remote sensors can detect different amounts of atmospheric information, from an information theory perspective. Academician Zeng Qingcun proposed the concept of the "Optimal Sensitivity Profile" in the early 1970s and systematically discussed the remote sensing of the atmosphere using infrared radiation information. He wrote a classic book titled "*Principles of Atmospheric Infrared Remote Sensing*" [3]. Rodgers pointed out that signal degrees of freedom and information entropy are two important parameters in retrieval theory [4]. By utilizing information entropy and degrees of freedom as evaluation criteria, a quantitative description was provided for the information capacity of atmospheric gas parameters contained in satellite hyperspectral detection data, aiming to assess the satellite's capability in atmospheric parameter retrieval. Subsequently, they have been widely applied in the analysis of satellite observation systems, such as the design, evaluation, and application of onboard atmospheric detection instruments. Fourrie et al. evaluated the information capacity before and after channel selection in an Atmospheric Infrared Sounder (AIRS) using information entropy and degrees of freedom as indicators and compared the performance differences between the hyperspectral AIRS and multispectral High-resolution Infrared Radiation Sounder (HIRS) instruments [5]. Collard used a stepwise iterative information entropy method combined with pre-screening conditions for channel selection in an Infrared Atmospheric Sounding Interferometer (IASI) [6]. Ventress and Dubhia optimized Collard's work and proposed a channel selection method that can quantitatively describe spectral correlation errors [7]. Hou Weizhen et al. conducted a preliminary study on the remote sensing of aerosol emissions in atmospheric pollution monitoring using static orbit hyperspectral detection and signal degrees of freedom as parameters [8]. Crevoisier observed the sensitive channel distribution of IASI for relevant gases by varying the perturbation gas concentrations [9]. Luo Shuang quantitatively described the retrieval capabilities of temperature, humidity, and ozone of the Fengyun-4A (FY-4A)/Geosynchronous Interferometric Infrared Sounder (GIIRS) by calculating information entropy and degrees of freedom [10]. Zheng Fengxun et al. introduced information content analysis tools to discuss the dependence of high-resolution cameras on observation angles and their retrieval capabilities and systematically and quantitatively described retrieval uncertainties [11]. Yang Yuhan et al. applied an information entropy stepwise iteration method to optimize the temperature detection channels of the GIIRS in the FY-4A interferometric atmospheric sounding instrument. Based on information entropy, they selected the channel with the richest temperature information in each iteration until the increment of information entropy contribution became flat, indicating that the channel configuration could reflect the temperature information detected by the instrument [12].

The FY-3D and FY-3E satellites are the second generation of polar-orbiting meteorological satellites developed by China. HIRAS-I is the first infrared hyperspectral instrument to be implemented on China's polar-orbiting meteorological satellites. FY-3E is the world's first meteorological satellite to operate in the dawn–dusk orbit, and HIRAS-II is a continuation of HIRAS-I [13]. Both FY-3D/HIRAS-I and FY-3E/HIRAS-II were developed by

the Shanghai Institute of Technical Physics, Chinese Academy of Sciences. In comparison to FY-3D/HIRAS-I, FY-3E/HIRAS-II features the integration of three spectral bands, increasing the number of spectral channels to 3041, thereby enhancing its Earth observation capabilities. The spectral and radiometric calibration accuracy, as well as radiation detection sensitivity, have also been correspondingly improved [14]. Only by fully understanding the information contained within the spectral range of FY-3D/HIRAS-I and FY-3E/HIRAS-II can we maximize the potential applications of the data. This paper utilizes the Rapid Radiative Transfer Model RTTOV to analyze and investigate the sensitivity of atmospheric gas composition perturbations and channel selection using the observed data from FY-3D/HIRAS-I and FY-3E/HIRAS-II in different experimental regions. Additionally, it calculates the degrees of freedom and information entropy for various atmospheric gas components included in both instruments to gain a more intuitive understanding of the retrieval capabilities of these two hyperspectral instruments for atmospheric parameters. The research findings play a crucial role in efficiently and effectively utilizing the vertical atmospheric profiling data from FY-3D/HIRAS-I and FY-3E/HIRAS-II. Furthermore, they hold significant implications for the design of future instruments and the application of satellite data retrieval.

The content of this paper is presented in the following sections. Section 1 is the introduction, which highlights the importance of the analysis and comparison of the detection capabilities of FY-3D/HIRAS-I and FY-3E/HIRAS-II based on information capacity. Section 2 introduces the instrument data and relevant models. Section 3 provides an overview of the data processing methods and experimental principles. Section 4 presents the results analysis. Finally, there are discussion and conclusion sections.

## 2. Data and Models

### *2.1. FY-3D/HIRAS-I*

FY-3D/HIRAS-I is the first infrared hyperspectral detection instrument to be utilized on China's polar-orbit meteorological satellites, with 2275 spectral channels, providing infrared radiation spectra in three spectral bands: long-wave infrared (LWIR), 650–1135 $cm^{-1}$; medium-wave infrared (MWIR) 1210–1750 $cm^{-1}$; and short-wave infrared (SWIR), 2155–2550 $cm^{-1}$ [15]. The instrument's design adopts the parallel observation of multiple small plane arrays, which can prolong the formation time of an interferogram at the same time and form an instantaneous field of view of Earth observation. Three small arrays simultaneously observe the same field of view of the target on the ground, and four different target areas are simultaneously observed by the small array detectors in each wave band. Each detector has an earth observation angle of 1.1°, the instantaneous field of view of the corresponding substellar point is about 16 km, and the ground distance between pixels is 26.17 km [16,17]. Specific performance parameters are shown in Table 1.

**Table 1.** FY-3D/HIRAS-I spectral characteristics and performance index.

| | **Wavenumber ($cm^{-1}$)** | **Spectral Resolution ($cm^{-1}$)** | **Number of Channels** |
|---|---|---|---|
| Spectral Characteristics | Long-Wave: 648.75–1134 | 0.625 | 781 |
| | Medium-Wave: 1208.5–1749.375 | 0.625 | 869 |
| | Short-Wave: 2153.75–2549.375 | 0.625 | 637 |
| Performance index | Scan cycle | 10 s | |
| | Field of view | 1.1° | |
| | Maximum scanning angle | ±50.4° | |
| | Radiometric calibration accuracy | 0.7 K | |
| | Spectral calibration accuracy | 7 ppm | |

The experimental areas were the African maritime region (−25° to 25°N, 50° to 95°E) and the Yangtze River Delta region in China (20° to 50°N, 100° to 130°E). The time periods for the experimental data were chosen to be 21 December 2021 to 18 January 2022 for the

African maritime region and 21 December 2021 to 4 January 2022 for the Yangtze River Delta region.

### 2.2. FY-3E/HIRAS-II

FY-3E/HIRAS-II is an Interferometric Fourier Transform Spectrometer (FTS) with an orbital height of 836km. The instrument operates in three infrared spectral bands: long-wave (LW), medium-wave (MW), and short-wave (SW), with a total of 3041 spectral channels. In the mid-to-long-wave infrared range of 3.92 to 15.38 μm, there are over 1370 spectral detection channels, and the highest spectral resolution can reach 0.625. Building upon the spectral product development of FY-3D/HIRAS-I, HIRAS-II improves the layout of the detector array within the Field of Regard (FOR) from a 2 × 2 arrangement to a 3 × 3 arrangement. The ground-viewing angular field of each pixel is 1° (compared to 1.1° in HIRAS-I), resulting in higher spatial resolution. The complete scanning cycle of HIRAS-II is 8 s, with a maximum scanning angle range of 100.8°, corresponding to an instantaneous field of view of approximately 14 km. This represents a significant improvement compared to FY-3D/HIRAS-I [14]. HIRAS-II has made significant advancements in detection sensitivity, spectral and radiometric quantification accuracy, as well as its operational lifespan, which contributes to further enhancing the accuracy of observational data. The detailed instrument parameter characteristics of HIRAS-II are presented in the Table 2 below:

**Table 2.** FY-3E/HIRAS-II spectral characteristics and performance index.

| | **Wavenumber ($cm^{-1}$)** | **Spectral Resolution ($cm^{-1}$)** | **Number of Channels** |
|---|---|---|---|
| Spectral Characteristics | Long-Wave: 650–1168.125 | 0.625 | 830 |
| | Medium-Wave: 1168.75–1920 | 0.625 | 1203 |
| | Short-Wave: 1920.625–2550 | 0.625 | 1008 |
| Performance index | Scan cycle | 8 s | |
| | Field of view | 1.1° | |
| | Maximum scanning angle | ±50.4° | |
| | Radiometric calibration accuracy | 0.4–1.0 K | |
| | Spectral calibration accuracy | 5 ppm | |

The experimental regions were the African oceanic region (25°–25°N, 50°–95°E) and the Chinese Yangtze River Delta terrestrial region (20°–50°N, 100°–130°E). The experimental data were collected from 21 December 2021 to 18 January 2022 for the African oceanic region and from 21 December 2021 to 4 January 2022 for the Chinese Yangtze River Delta terrestrial region.

### 2.3. Reanalysis Data

In this experiment, partial atmospheric parameter profiles and surface parameters from the European Centre for Medium-Range Weather Forecasts (ECMWF) Atmospheric Composition Reanalysis 4 (EAC4) dataset were used as input information for RTTOV to retrieve simulated brightness temperature values. The experiment data were taken during the same time period as the satellite observations. The EAC4 dataset has a temporal resolution of 3 h and is divided into 25 atmospheric levels (https://ads.atmosphere.copernicus.eu/cdsapp#!/dataset/cams-global-reanalysis-eac4 (accessed from 21 December 2021 to 18 January 2022)).

Due to the absence of $CO_2$ reanalysis data in EAC4, for this experiment, the $CO_2$ profile data from the ECMWF EGG4 dataset (This dataset is part of the ECMWF Atmospheric Composition Reanalysis focusing on long-lived greenhouse gases: carbon dioxide ($CO_2$) and methane ($CH_4$)) were used as input information for RTTOV to obtain simulated brightness temperature values. This dataset has slower temporal updates, but the interannual variation in $CO_2$ gas levels remains relatively stable. Therefore, the EGG4 data used in this experiment represent the average of recent years.

Due to the difficulty in obtaining $N_2O$ reanalysis data, when performing forward simulations using RTTOV, Whole Atmosphere Community Climate Model (WACCM) data are used for $N_2O$ instead.

### *2.4. Forecast Data*

For this experiment, WACCM global climate model data (https://rda.ucar.edu/datasets/ds313.6/dataaccess/ (accessed from 21 December 2021 to 18 January 2022)) were used as background field data to calculate the background error covariance. The spatial resolution of the WACCM dataset is $0.9^\circ \times 1.25^\circ$, with a temporal resolution of 6 h. The dates of the experimental data align with those of the satellite observation.

### *2.5. RTTOV Radiative Transfer Model*

The RTTOV fast radiative transfer model is developed from the fast radiative transfer model of TOVS. RTTOV can rapidly and accurately simulate the observed brightness temperature of various satellite instruments under given atmospheric state parameter conditions. It can also quickly calculate the Jacobian matrices, which represent the sensitivity of observed radiance to atmospheric states (such as temperature and absorbing gases). The experiment utilized RTTOV version 13, and the sensor coefficient files and emissivity files for FY-3D/HIRAS-I and FY-3E/HIRAS-II were obtained from the official website for conducting radiative transfer simulations. In this experiment, RTTOV was primarily used for forward simulations, and the input data are shown in Table 3.

**Table 3.** Input Parameters for Clear-Sky RTTOV Radiative Transfer Simulation.

| Type of Data | | | |
|---|---|---|---|
| Atmospheric Parameters | Layered Pressure | hPa | EAC4 |
| | Temperature | K | EAC4 |
| | Humidity | Kg/kg | EAC4 |
| | Ozone | Kg/kg | EAC4 |
| | Carbon Monoxide | Kg/kg | EAC4 |
| | Methane | Kg/kg | EAC4 |
| | Carbon Dioxide | Kg/kg | EGG4 |
| | Nitrous Oxide | Kg/kg | WACCM |
| Surface Parameters | Land Surface | | HIRAS-I/HIRAS-II |
| | Elevation | m | HIRAS-I/HIRAS-II |
| | Surface Emissivity Dataset | | RTTOV |
| | Surface Temperature | K | EAC4 |
| | Sea Surface Temperature | K | EAC4 |
| | 2 m Temperature | K | EAC4 |
| | 2 m Dew Point Temperature | K | EAC4 |
| | 10 m Wind U Component | m/s | EAC4 |
| | 10 m Wind V Component | m/s | EAC4 |

## 3. Principle, Method, and Steps

Before conducting the selection of atmospheric gas component channels and the analysis of retrieval capability, we need to process the FY-3D/HIRAS-I observation data, FY-3E/HIRAS-II observation data, EAC4 reanalysis data, EGG4 reanalysis data, and WACCM forecast data. This includes truncating and selecting clear-sky scenes from HIRAS-I/HIRAS-II L1 observation data, interpolating reanalysis and forecast data, and standardizing the units of gas concentrations. After the data processing is completed, we input it into the RTTOV fast radiative transfer model for forward calculation, obtaining simulated brightness temperatures. Then, we conduct sensitivity analysis on the gases in each channel to determine the range of strongly sensitive wavelengths. Next, channel selection is performed to choose channels suitable for each gas. Finally, we calculate the information

capacity of each gas and conduct comparative analysis. The overall roadmap is shown in the following Figure 1:

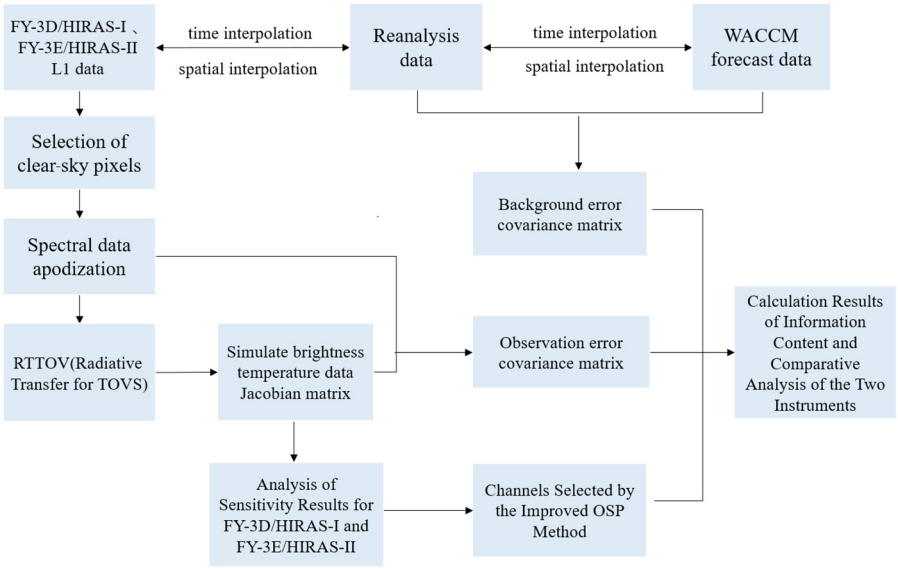


**Figure 1.** The overall experimental roadmap.

### *3.1. Processing of FY-3D/HIRAS-I and FY-3E/HIRAS-II Observation Data*

#### 3.1.1. Radiance-to-Brightness Temperature Conversion and Truncation

The radiance values are converted to brightness temperature values using the Planck radiance formula. For a temperature of $T$ and a wavelength of $\lambda$, the Planck spectral radiance formula [18] is given by:

$$M_\lambda(T) = \frac{2\pi hc^2}{\lambda^5(e^{hc/\lambda kT} - 1)} = \frac{c_1}{\lambda^5(e^{c_2/\lambda T} - 1)}, \quad (1)$$

where $M_\lambda(T)$ represents the spectral radiance of a blackbody (radiant flux density), $h$ is the Planck constant, $k$ is the Boltzmann constant, $c_1$ is the first radiation constant, and $c_2$ is the second radiation constant.

The Planck radiance formula is:

$$B_\lambda(T) = \frac{2hc^2}{\lambda^5(e^{hc/\lambda kT} - 1)}, \quad (2)$$

If the Planck radiance is expressed in wavenumber $\nu$, the formula becomes:

$$B_v(T) = \frac{2hc^2v^5}{e^{hcv/kT} - 1}, \quad (3)$$

From the above two equations, the blackbody brightness temperature $T$ is obtained as:

$$T = \frac{hcv/k}{\ln(2hc^2v^5/B_v(T) + 1)}, \quad (4)$$

The Level 1 observation data of HIRAS-I/HIRAS-II are not processed by apodization and require apodization in practical applications to reduce the side lobe effects [19]. In this study, a Hamming function is used for apodization. The solid black line represents the spectral brightness temperature data not processed by apodization, while the solid red line represents the apodization spectral brightness temperature. From Figure 2, it can be observed that both FY-3D/HIRAS-I and FY-3E/HIRAS-II spectra are smoother and exhibit fewer spikes after apodization.

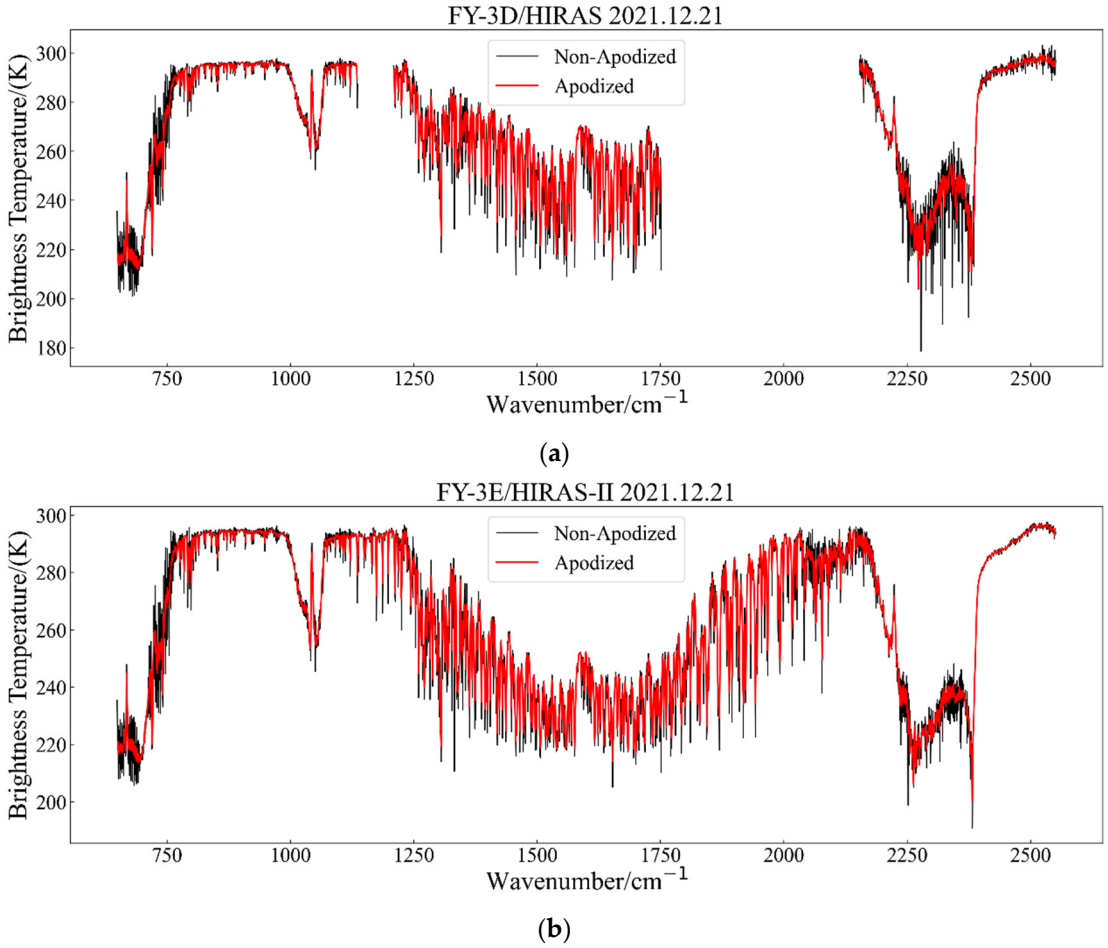


**Figure 2.** Comparison of spectral brightness temperature before and after apodization: (**a**) FY-3D/HIRAS-I; (**b**) FY-3E/HIRAS-II.

#### 3.1.2. Clear-Sky Selection

Because the RTTOV fast radiative transfer model does not provide high simulation accuracy under cloudy conditions, the sample data selected for this experiment were all clear-sky scenes. The criteria for determining clear-sky samples were as follows: We selected the observation data from five representative infrared channels (810 cm$^{-1}$, 830 cm$^{-1}$, 850 cm$^{-1}$, 870 cm$^{-1}$, 890 cm$^{-1}$) in the long-wave region. The spectral brightness temperature of these channels should be greater than 290 K, and the deviation between the observed spectral brightness temperature and the simulated spectral brightness temperature for the corresponding window channel should be less than 5 K.

### *3.2. Processing of EAC4 and EGG4 Reanalysis Data*

The EAC4 and EGG4 reanalysis data have different temporal and spatial resolutions compared to HIRAS-I and HIRAS-II. Therefore, we need to interpolate the reanalysis data to match the temporal and spatial grids of the satellite observations. For temporal interpolation, we used the satellite observation data as the reference and perform linear interpolation using the two closest reanalysis data points in time. As for spatial interpolation, we employ a cubic spline interpolation algorithm, taking into account the geographical location information of the satellite observation data to interpolate the reanalysis data.

### *3.3. Processing of WACCM Forecast Data*

The WACCM forecast data also have different temporal and spatial resolutions compared to HIRAS-I and HIRAS-II, so interpolation is required for the forecast data as well.

The interpolation methods for both time and space are consistent with those used for reanalysis data.

### *3.4. Conversion between Units of kg/kg and mol/mol*

The EAC4 and EGG4 reanalysis data have gas concentration units in kg/kg, while the WACCM forecast data have gas concentration units in mol/mol. Therefore, unit conversion is necessary. Kg/kg represents the mass ratio of gas to air, while mol/mol represents the molar ratio of gas to air. Taking $O_3$ as an example, the expressions for kg/kg and mol/mol are as follows:

$$\frac{\mathrm{kg}(O_3)}{\mathrm{kg}(AIR)} = \frac{\mathrm{mol}(O_3)}{\mathrm{mol}(AIR)} \times \frac{\mathrm{kg}(O_3)}{\mathrm{mol}(O_3)} \div \frac{\mathrm{kg}(AIR)}{\mathrm{mol}(AIR)}, \tag{5}$$

where *AIR* refers to air, g/mol represents molar mass, and the molar mass of O-16 is 48 g/mol. The molar mass of air is 28.9634 g/mol. Therefore, we can obtain the unit conversion formula as follows:

$$\frac{\mathrm{kg}(O_3)}{\mathrm{kg}(AIR)} = \frac{\mathrm{mol}(O_3)}{\mathrm{mol}(AIR)} \times (0.048\mathrm{kg/mol}) \div (0.0289634\mathrm{kg/mol}), \tag{6}$$

The final formula is:

$$\mathrm{kg/kg} = (\mathrm{mol/mol}) \times 1.657, \tag{7}$$

Other gases follow the same principle.

### *3.5. Simulation of Spectral Sensitivity for FY-3D/HIRAS-I and FY-3E/HIRAS-II Observations*

For this experiment, the input data for the RTTOV radiative transfer model were obtained by combining FY-3D/HIRAS-I L1 observational data, FY-3E/HIRAS-II L1 observational data, EAC4 reanalysis data (including T, $H_2O$, $O_3$, CO, and $CH_4$ data), EGG4 reanalysis data ($CO_2$ data), and $N_2O$ data from the WACCM forecast profile data. The sensor coefficient files provided by the official RTTOV website for FY-3D/HIRAS-I and FY-3E/HIRAS-II were used. The brightness temperature values for each channel of HIRAS-I and HIRAS-II were calculated. Then, perturbations were applied to the retrieval accuracy of various gas parameters, including T (1K), $H_2O$ (20%), $O_3$ (10%), CO (10%), $CO_2$ (1%), $CH_4$ (10%), $N_2O$ (2%), and $T_{surf}$ (1K). The brightness temperature perturbation value was calculated using the following equation [20] to represent the response of each channel to the perturbation of atmospheric parameters:

$$S_{\mathrm{j}}(v_1) = BT(X_0 + \delta X_j) - BT(X_0), \tag{8}$$

In the equation, $S_{\mathrm{j}}(v_1)$ represents the simulated brightness temperature change for each channel before and after the perturbation of the aforementioned atmospheric parameters, measured in Kelvin (K). *BT* is the simulated brightness temperature obtained using the RTTOV radiative transfer model. $X_0$ is the atmospheric parameters before the perturbation, and $\delta X_j$ is the perturbation magnitude of the atmospheric gas composition parameter j.

### *3.6. Calculation of Observation Error Covariance*

In satellite remote sensing observations, the main sources of observation error are the errors introduced by the instrument and the errors associated with the radiative transfer model. It is generally assumed that the different channels are uncorrelated; thus, the observation error covariance matrix is a diagonal matrix [10]. The calculation formula for the diagonal elements [19] is as follows:

$$\varepsilon = \sqrt{\frac{\sum (Y^m - F(x))^2}{n-1}}, \tag{9}$$

where $Y^m$ represents the observed brightness temperature from FY-3D/HIRAS-I and FY-3E/HIRAS-II, $m$ is the number of selected channels, $F(x)$ represents the simulated brightness

temperature calculated by the RTTOV radiative transfer model, and $n$ represents the number of samples.

### *3.7. Calculation of Background Error Covariance*

The background error covariance matrix describes the errors and correlations between the predicted values and the true values of various atmospheric state vectors [21]. The background error covariance matrix is denoted as $B$ and is represented as follows:

$$B = \begin{pmatrix} b_{11} & \cdots & b_{1j} \\ \vdots & \ddots & \vdots \\ b_{i1} & \cdots & b_{ij} \end{pmatrix},$$

where $b_{ij}$ represents the error covariance between the background fields of the $i$-th and $j$-th layers [22]. The formula is:

$$b_{ij} = \mathrm{cov}(X^i, X^j) = \frac{1}{n}\sum_{k=1}^{n}[(X_k^i - E(X^i)) \times (X_k^i - E(X^j))], \tag{10}$$

where $X$ represents the error between the background field and the true field. $X_k^i$ represents the data for the $k$-th sample in the $i$-th layer. $E(X^i)$ represents the mean forecast error for the $i$-th layer. $n$ represents the number of samples.

### *3.8. Channel Selection Method*

After performing the simulation of spectral sensitivity for FY-3D/HIRAS-I and FY-3E/HIRAS-II and determining the spectral positions of each gas-sensitive channel, channel selection is conducted as a basis for calculating signal degrees of freedom and Shannon information. For channel selection, we based our approach on the Optimal Sensitivity Profile method (OSP) proposed by Crevoisier for selecting $CO_2$ channels in AIRS [23] and made some improvements to it. The original algorithm used one-tenth of the signal-to-noise ratio of the first channel at each pressure level as the threshold to remove channels with Jacobian peaks at the same height but with a signal-to-noise ratio below the threshold. However, in our experiments, we found that the signal-to-noise ratio difference between adjacent channels was not significant, so there was no need to use one-tenth as the threshold. Instead, we directly used the signal-to-noise ratio of the first channel at each pressure level as the threshold to remove channels with Jacobian peaks at the same height but with a signal-to-noise ratio below this threshold. This approach allows us to remove more similar channels, avoiding redundant information and excessive repetition of channels.

The specific criteria for channel selection are as follows: (1) The target signal within the same channel must be greater than the background interference signal (signals caused by other variables). The target signal should be as high as possible, while the detector noise and calibration errors should be minimized. This criterion can be related to the relationship between the brightness temperature difference before and after the target gas perturbation and the instrumental parameters (noise, sensitivity, calibration, etc.); (2) The selected channels should cover the entire atmospheric layer as much as possible. This criterion can be related to the uniform and narrow distribution of the Jacobian peaks of the target gas calculated by the radiative transfer model throughout the atmospheric layer. The signal-to-noise ratio is defined as the ratio of the target signal to the background interference signal. The signal is defined as the brightness temperature variation caused by the target gas, while the noise is defined as the brightness temperature variation caused by other variables within the same channel.

To avoid high signal-to-noise ratio channels caused by weak responses of target signals and lower responses of interference signals, it is necessary to define a threshold to directly remove such channels. This threshold is defined as the instrument's Noise Equivalent Delta Temperature (NEDT), which represents the minimum detectable temperature difference. The perturbation value of the target signal must be greater than the instrument's sensitivity,

which is then used to calculate the signal-to-noise ratio. The NEDT values are obtained from the downloaded FY-3D/HIRAS-I L1 and FY-3E/HIRAS-II L1 data files provided by the National Satellite Meteorological Center.

The specific steps for channel selection are as follows: (1) calculate the signal-to-noise ratio (SNR) and remove channels where the target gas has an SNR lower than the NEDT threshold; (2) save the Jacobian profiles of the target gas obtained from the RTTOV fast radiative transfer model then select the channel with the maximum Jacobian value at each pressure level as the first channel for that level; (3) apply the improved OSP (Optimal Sensitivity Profile) algorithm to select the channels.

### *3.9. Information Capacity Calculation*

Based on the aforementioned calculations of the simulated brightness temperature, observation error covariance matrix, background error covariance matrix, and Jacobian matrix, the information capacity is computed. ER and DFS are both quantitative indicators for assessing retrieval capability and remote sensing system performance. ER is related to the spectral characteristics and performance of the instrument. It can quantify the reduction in uncertainty of the observed values caused by retrieval. However, a high-precision scalar and a set of low-precision vector data may have the same ER. Therefore, DFS are also needed for evaluation [24]. DFS represent the independent signals contained in the measurement vector or measurement space. The higher the DFS, the more comprehensive the independent information included in the observation. When the DFS for a particular parameter exceed 0.5, it can be considered that the parameter can be obtained through retrieval based on the observations [21]. The higher the DFS and ER, the more information is contained in the observations, indicating a stronger ability of the satellite instrument to invert parameters. Their specific descriptions are as follows:

Menke defined the average kernel function [25] as:

$$A = (K^T S_\varepsilon^{-1} K + S_{ap}^{-1})^{-1} K^T S_\varepsilon^{-1} K, \tag{11}$$

where $K$ represents the Jacobian matrix, $S_\varepsilon$ is the observation error covariance matrix, $S_{ap}$ is the background error covariance matrix, and $T$ and $-1$ denote the transpose and inverse of the matrices, respectively.

$$DFS = Trace(I - \hat{S} S_{ap}^{-1}), \tag{12}$$

where $S_{ap}$ is the background error covariance matrix, and $\hat{S}$ is the post-observation error covariance matrix.

ER and $\hat{S}$ formulas [11] are:

$$\hat{S} = (K^T S_\varepsilon^{-1} K + S_{ap}^{-1})^{-1}, \tag{13}$$

$$ER = \frac{1}{2} \ln |S_{ap}^{-1}| - \frac{1}{2} \ln |\hat{S}|, \tag{14}$$

## 4. Experimental Results Analysis

### *4.1. Analysis of Sensitivity Results for FY-3D/HIRAS-I and FY-3E/HIRAS-II*

Using RTTOV as the fast radiative transfer model and based on the method described in Section 3.5 (Equation (8)), we obtained the relevant results as shown in the following figures:

As can be seen from Figures 3 and 4, the channel sensitivities of the atmospheric profiles for FY-3D/HIRAS-I and FY-3E/HIRAS-II are basically consistent. Temperature and water vapor variations exhibit the strongest sensitivities, which differ in different experimental regions. On the other hand, the sensitivities of other gases remain relatively stable, with minor differences in sensitivity observed across different experimental regions.

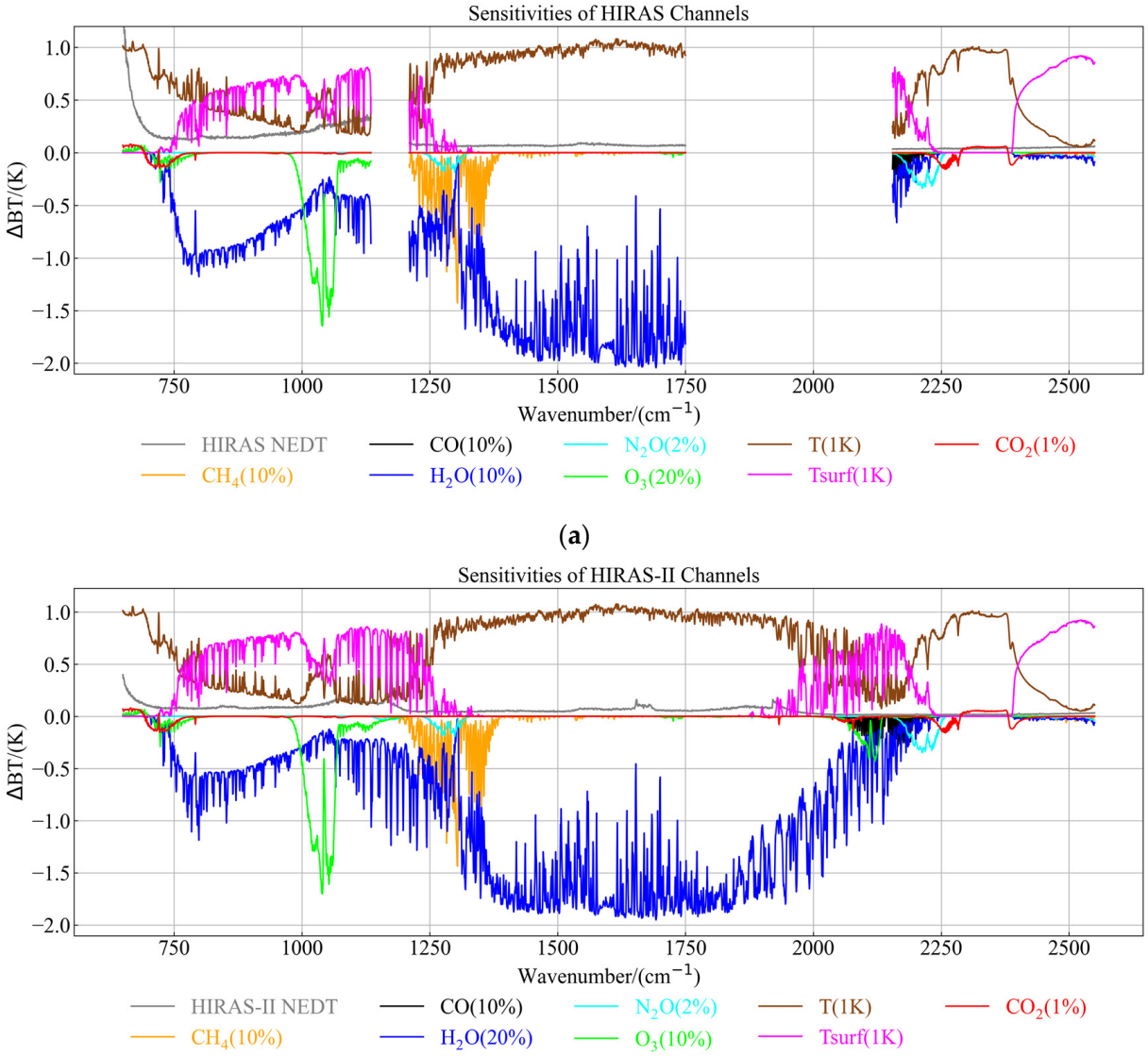


**Figure 3.** Sensitivity analysis of various gas channels in the African oceanic region: (**a**) FY-3D/HIRAS-I; (**b**) FY-3E/HIRAS-II.

For temperature, in the long-wave infrared region, the sensitivity is stronger in the 650–750 cm$^{-1}$ band with brightness temperature variations of 0.5–1 K. However, the sensitivity decreases in the 750–1250 cm$^{-1}$ band, with brightness temperature variations within 0.5 K. In the mid–short-wave region, except for weak sensitivity in the 2070–2130 cm$^{-1}$ and 2375–2500 cm$^{-1}$ bands, the remaining bands exhibit the strongest sensitivity, with brightness temperature variations around 1 K. This indicates that temperature disturbances have the greatest impact on this particular region.

For water vapor, in the long-wave infrared region, the sensitivity is weaker in the 650–750 cm$^{-1}$ band with brightness temperature variations within 0.5 K. The sensitivity gradually increases in the 750–1250 cm$^{-1}$ band with brightness temperature variations of 0.5–1.2 K. In the mid–short-wave infrared region, the strongest sensitivity for water vapor is in the 1230–2000 cm$^{-1}$ band, with brightness temperature variations around 2 K, which is higher than in other regions. This indicates that water vapor disturbances have the greatest impact on this band. However, the sensitivity is poorest in the 2250–2500 cm$^{-1}$ band, with brightness temperature variations close to 0.

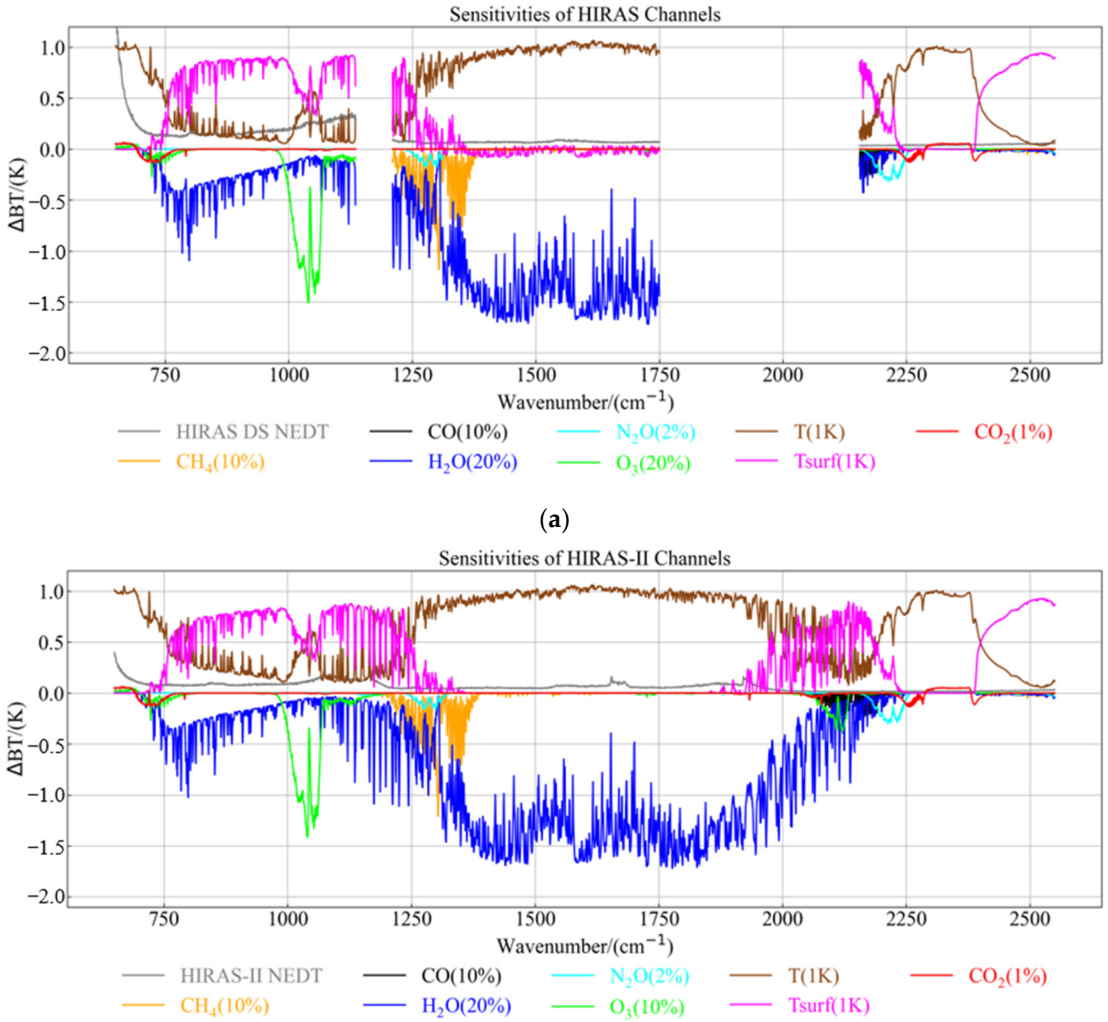


**Figure 4.** Sensitivity analysis of various gas channels in the Chinese Yangtze River Delta region: (**a**) FY-3D/HIRAS-I; (**b**) FY-3E/HIRAS-II.

For ozone, FY-3E/HIRAS-II has an additional region with strong variations compared to FY-3D/HIRAS-I. In the short-wave infrared region, the sensitivity is significant in the 2120–2125 cm$^{-1}$ band with brightness temperature variations within 0.5 K. The other two regions with strong variations are in the long-wave infrared region, specifically the 725–750 cm$^{-1}$ and 1000–1125 cm$^{-1}$ bands. The sensitivity is smaller in the 725–750 cm$^{-1}$ band, with brightness temperature variations around 0.3 K. The sensitivity is highest in the 1000–1125 cm$^{-1}$ band, with brightness temperature variations around 1.5 K. This indicates that ozone disturbances have the greatest impact on this part of the spectrum.

For methane, the maximum sensitivity is in the 1250–1375 cm$^{-1}$ band with brightness temperature variations within 1.5 K. For nitrous oxide, the sensitivity is significant in the 1250–1300 cm$^{-1}$ band with brightness temperature variations within 0.2 K. The maximum sensitivity is in the 2125–2250 cm$^{-1}$ band with brightness temperature variations within 0.4 K. For carbon monoxide, the maximum sensitivity is in the 2120–2140 cm$^{-1}$ band with brightness temperature variations within 0.3 K. For carbon dioxide, the strongest sensitivity is in the 730–750 cm$^{-1}$, 2245–2255 cm$^{-1}$, and 2380–2400 cm$^{-1}$ bands with brightness temperature variations within 0.3 K.

### *4.2. Jacobian Matrix*

The weight function reflects the sensitivity of satellite-observed radiance to the vertical profiles of target components. The Jacobian matrix used in the experiment is computed using the K-matrix module provided by the RTTOV fast radiative transfer model. The Jacobian primarily represents the sensitivity of atmospheric gas components at different pressure levels and within different spectral bands. The normalized Jacobian weight functions are shown below.

Figures 5 and 6 display the Jacobian matrices of normalized mode calculated for gases $O_3$, $CH_4$, CO, $CO_2$, and $N_2O$ in the 650–2550 $cm^{-1}$ wavelength range. The horizontal axis represents wave numbers, the vertical axis represents pressure, and the color gradient indicates the sensitivity level. It can be observed that the sensitivity of different gases varies across different pressure levels and spectral bands. From the figures, it can be seen that the peak values of the weight functions for these gases are mainly concentrated in the middle-to-upper atmosphere (700–10 hPa), indicating that the optimal information layers observed by these two satellites are primarily located in the upper atmosphere. Gaseous $O_3$ exhibits peak weight function values at around 200–10 hPa, gaseous $CH_4$ shows peak values at around 700–200 hPa, gaseous CO exhibits peak values at around 700–200 hPa, gaseous $CO_2$ has its weight function maximum concentrated at around 200–20 hPa, and gaseous $N_2O$ shows its peak weight function values concentrated at around 300–20 hPa. Different satellite observations at different wavelengths exhibit varying sensitivities to the vertical distribution of atmospheric gas components. A reasonable selection of channel combinations can incorporate more information about the distribution of target components in the atmosphere, thus improving the accuracy of retrieval. However, too many channels can reduce computational efficiency and may result in information redundancy. The Jacobian results from Figures 4 and 5 show that the ideal retrieval bands for $O_3$, $CH_4$, CO, $CO_2$, and $N_2O$ are the same as those in Figures 2 and 3.

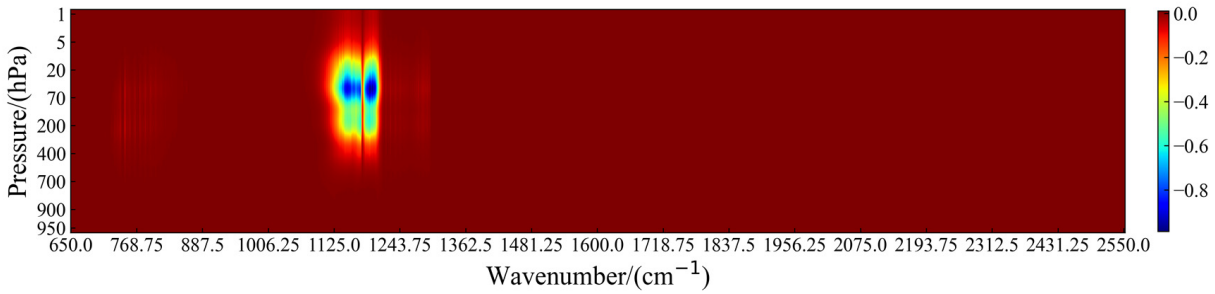


(**a**)

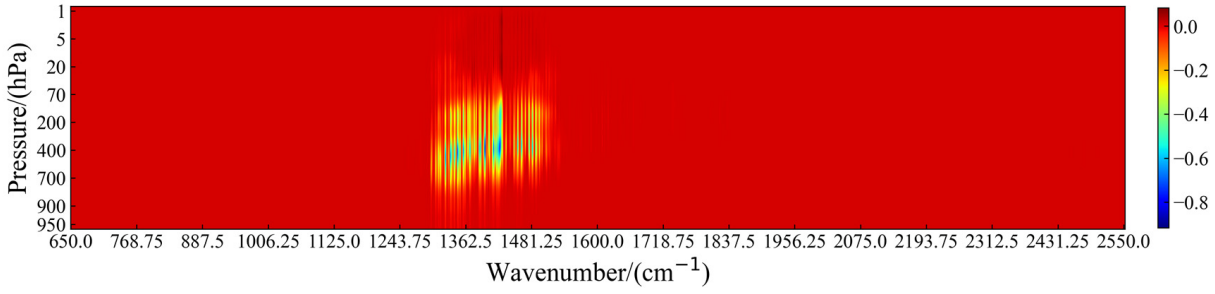


(**b**)

**Figure 5.** *Cont.*

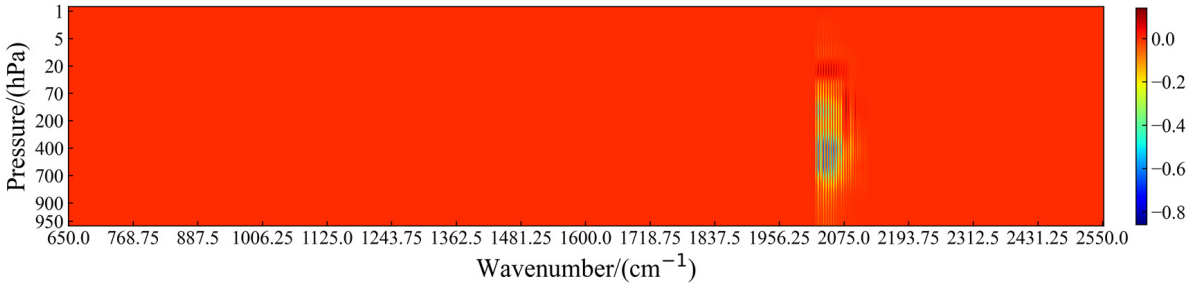


(**c**)

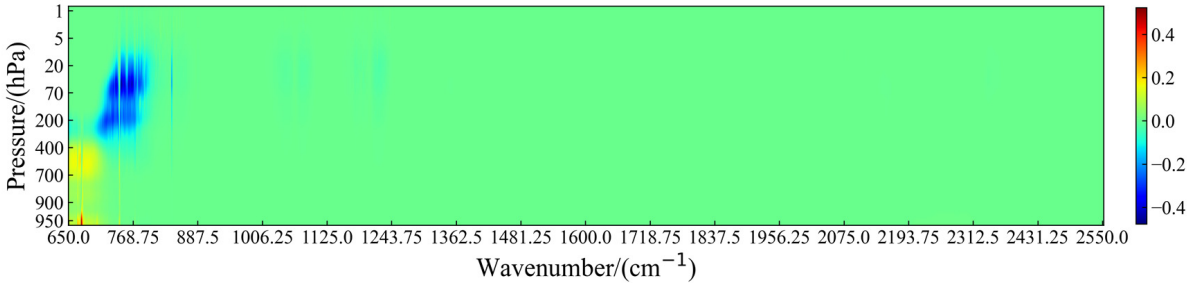


(**d**)

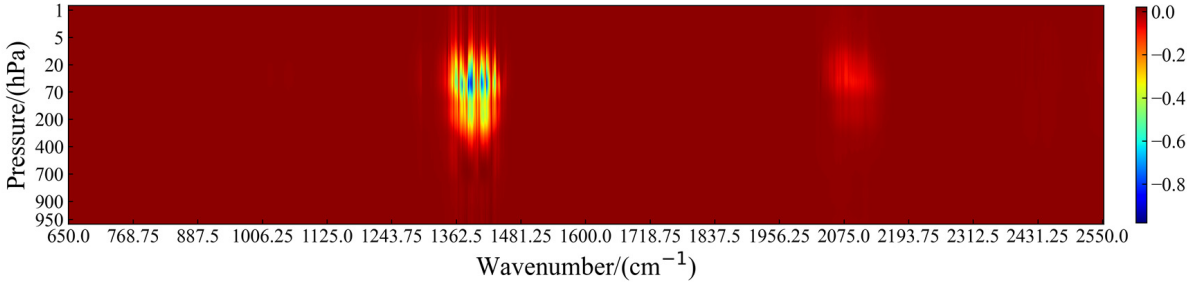


(**e**)

**Figure 5.** The Jacobian altitude and distribution of sensitive channels for FY-3D/HIRAS-I: (**a**) $O_3$; (**b**) $CH_4$; (**c**) CO; (**d**) $CO_2$; (**e**) $N_2O$.

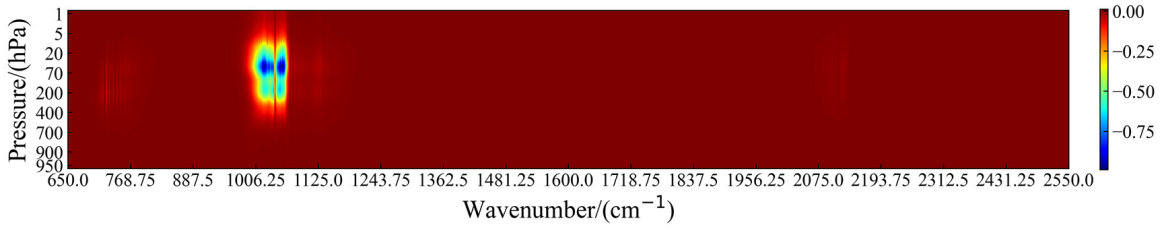


(**a**)

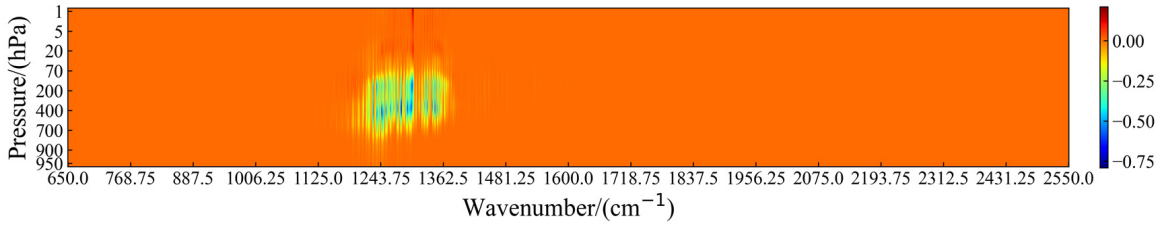


(**b**)

**Figure 6.** *Cont.*

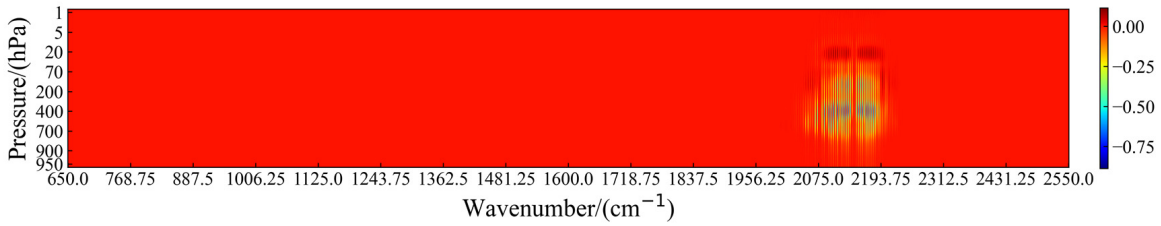


(**c**)

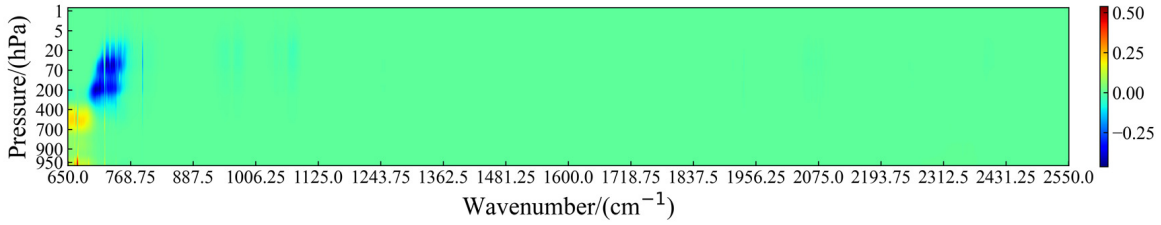


(**d**)

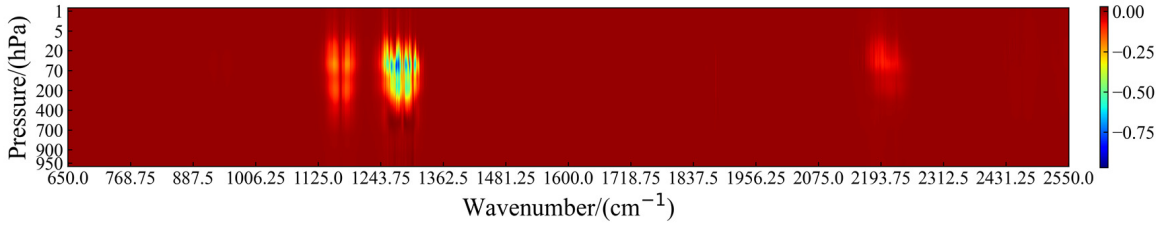


(**e**)

**Figure 6.** The Jacobian altitude and distribution of sensitive channels for FY-3E/HIRAS-II: (**a**) $O_3$; (**b**) $CH_4$; (**c**) CO; (**d**) $CO_2$; (**e**) $N_2O$.

### *4.3. Channels Selected by the Improved OSP Method*

Based on the channel selection method described in Section 3.8, the channels for each gas were selected separately for FY-3D/HIRAS-I and FY-3E/HIRAS-II. The selected channels for each gas are as follows (Figures 7–13):

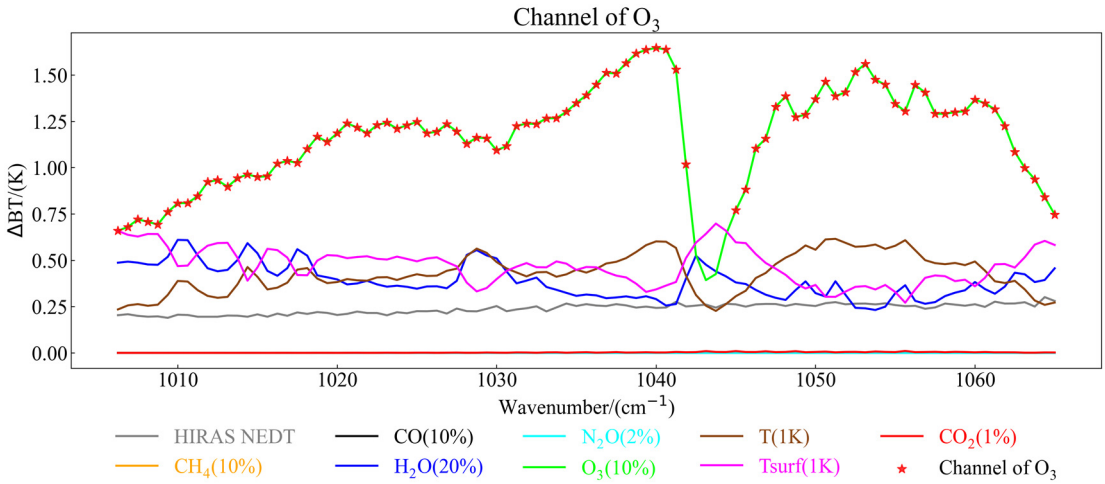


(**a**)

**Figure 7.** *Cont.*

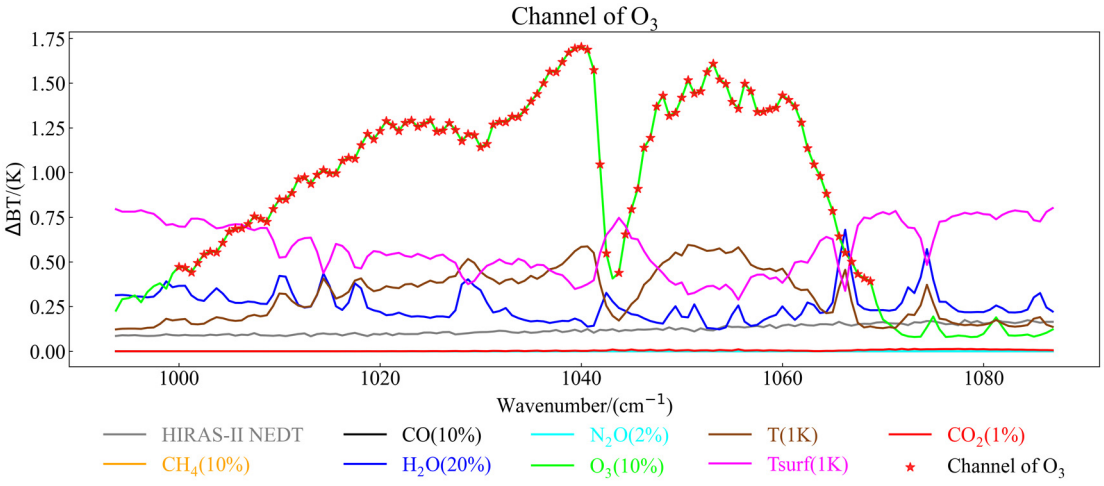


(**b**)

**Figure 7.** Results of $O_3$ channel selection: (**a**) FY-3D/HIRAS-I; (**b**) FY-3E/HIRAS-II.

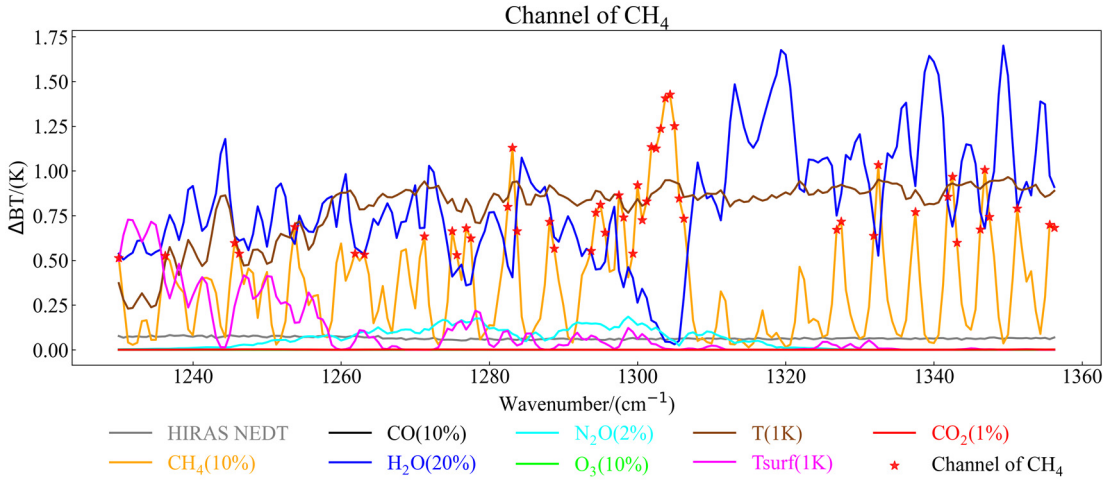


(**a**)

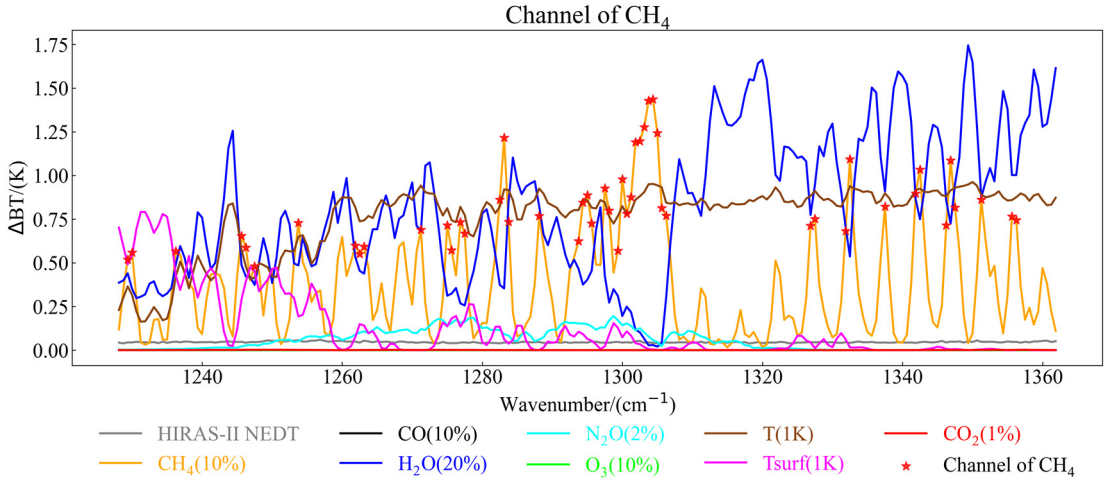


(**b**)

**Figure 8.** Results of $CH_4$ channel selection: (**a**) FY-3D/HIRAS-I; (**b**) FY-3E/HIRAS-II.

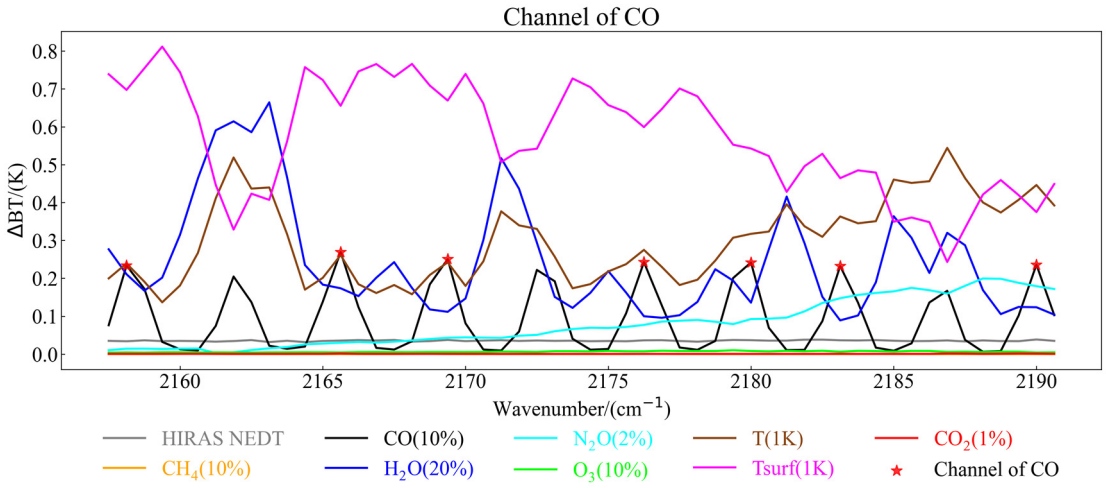


(**a**)

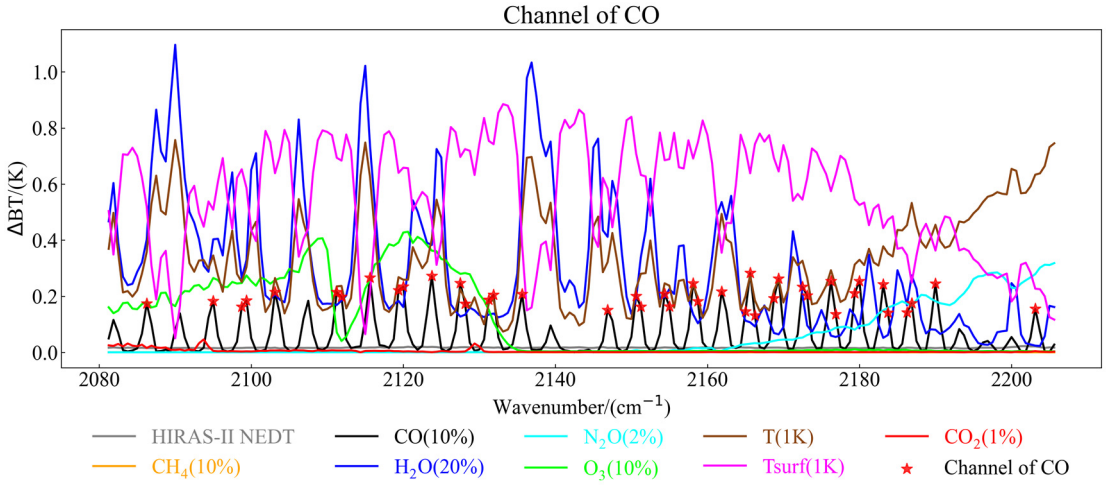


(**b**)

**Figure 9.** Results of CO channel selection: (**a**) FY-3D/HIRAS-I; (**b**) FY-3E/HIRAS-II.

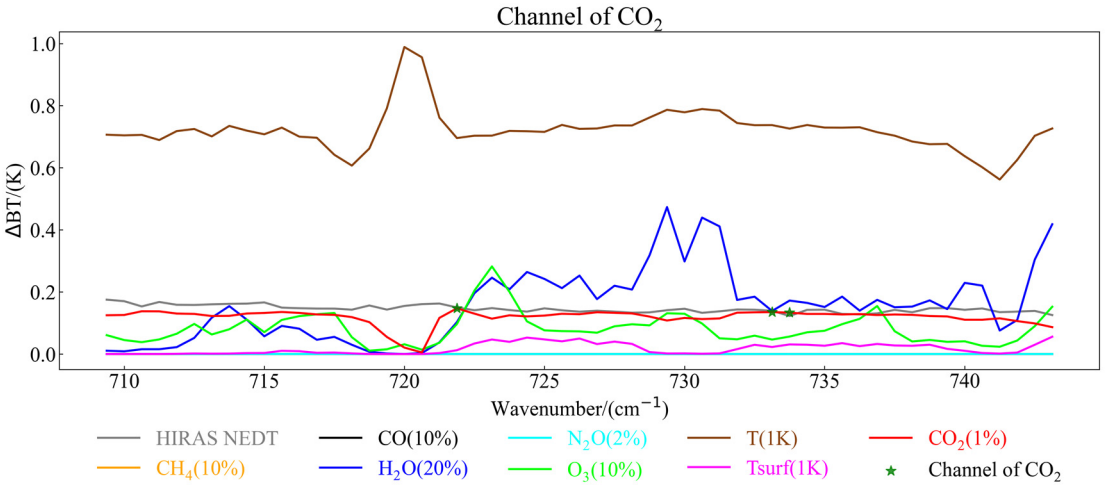


(**a**)

**Figure 10.** *Cont.*

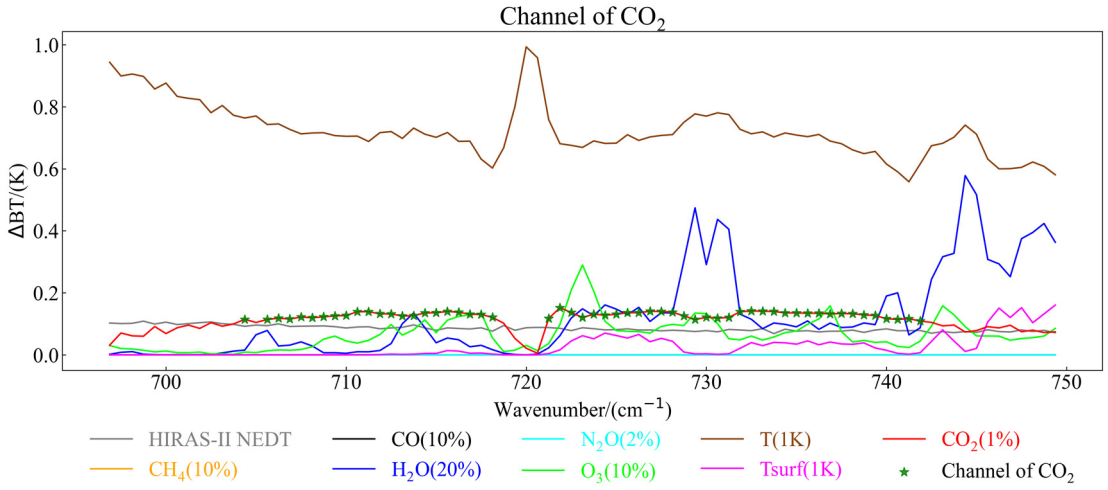


(**b**)

**Figure 10.** Results of long-wave infrared channel selection for $CO_2$: (**a**) FY-3D/HIRAS-I; (**b**) FY-3E/HIRAS-II.

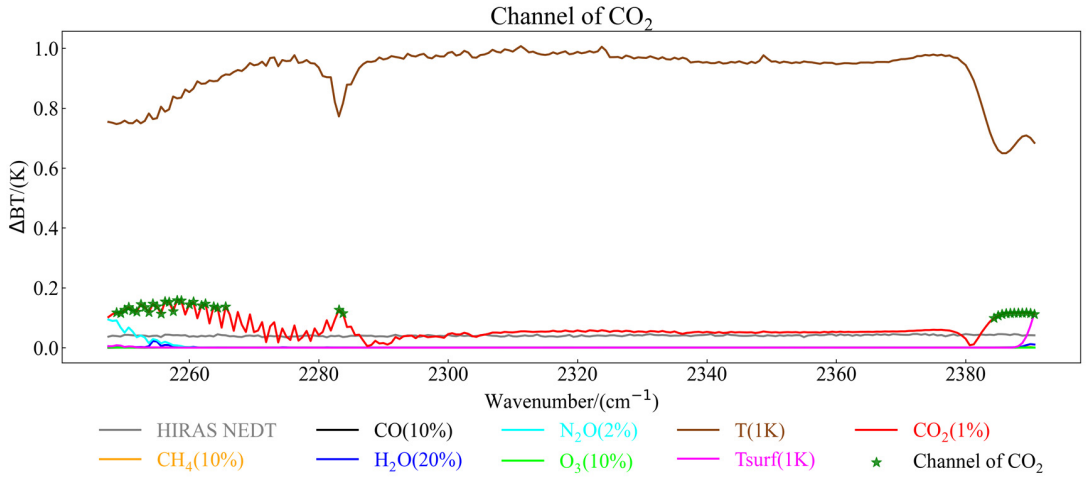


(**a**)

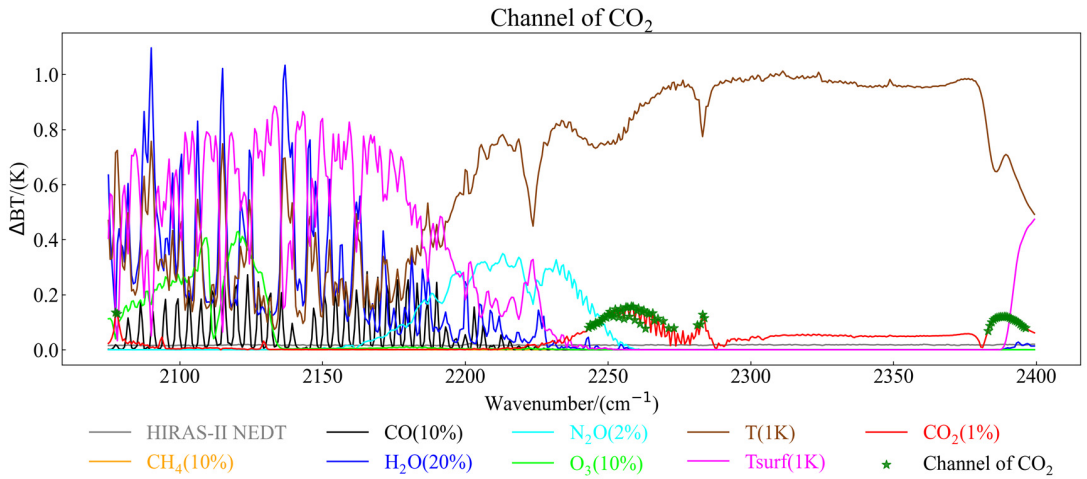


(**b**)

**Figure 11.** Results of short-wave infrared channel selection for $CO_2$: (**a**) FY-3D/HIRAS-I; (**b**) FY-3E/HIRAS-II.

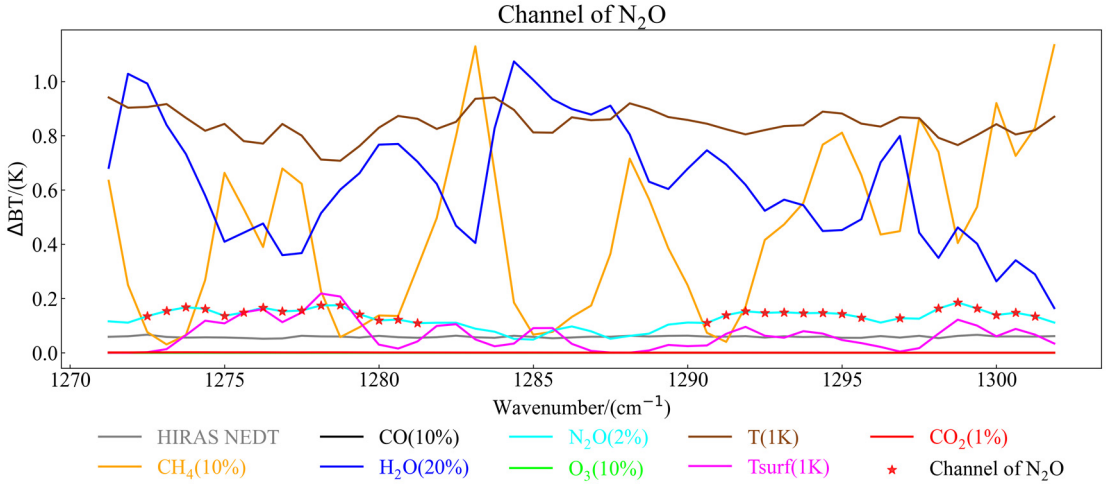


(**a**)

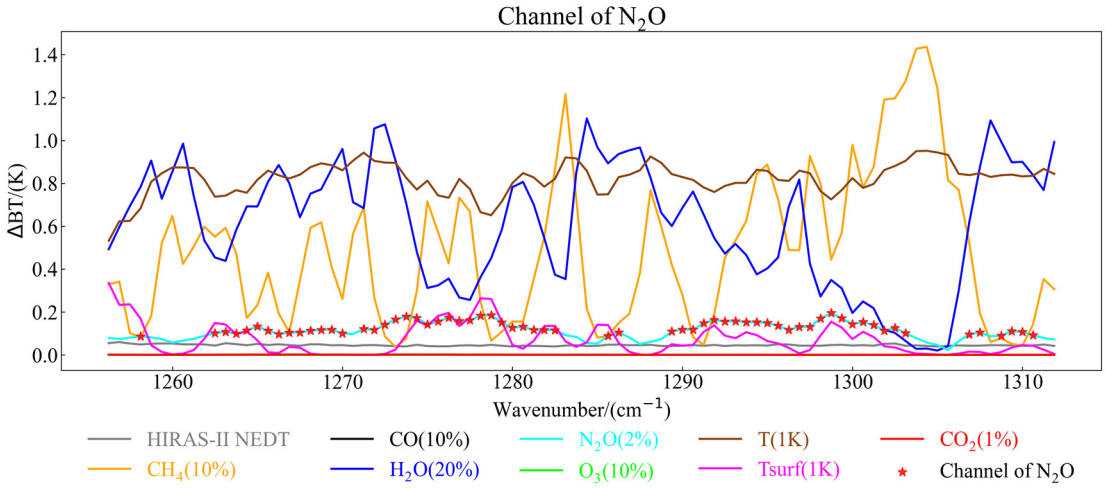


(**b**)

**Figure 12.** Results of long-wave infrared channel selection for $N_2O$: (**a**) FY-3D/HIRAS-I; (**b**) FY-3E/HIRAS-II.

The final channel selection results are as follows: FY-3D/HIRAS-I has a total of 91 ozone channels selected, while FY-3E/HIRAS-II has a total of 110 ozone channels selected. For methane, FY-3D/HIRAS-I has 49 selected channels, and FY-3E/HIRAS-II has 50 selected channels. The total number of carbon monoxide channels is 7 for FY-3D/HIRAS-I and 41 for FY-3E/HIRAS-II. In the case of long-wave carbon dioxide channels, FY-3D/HIRAS-I has 3 selected channels, while FY-3E/HIRAS-II has 56 selected channels. For short-wave carbon dioxide channels, FY-3D/HIRAS-I has 32 selected channels, while FY-3E/HIRAS-II has 69 selected channels. The total number of long-wave nitrous oxide channels is 31 for FY-3D/HIRAS-I and 64 for FY-3E/HIRAS-II. As for short-wave nitrous oxide channels, FY-3D/HIRAS-I has 104 selected channels, while FY-3E/HIRAS-II has 127 selected channels. It can be observed that FY-3E/HIRAS-II has a higher number of selected channels compared to FY-3D/HIRAS-I.

### *4.4. Calculation Results of Information Content and Comparative Analysis of the Two Instruments*

Based on the calculated Jacobian matrices, observation error covariance matrices, and background error covariance matrices, the DFS and ER were calculated using Equations (11)–(14). The DFS and ER for each atmospheric gas component of FY-3D/HIRAS-I and FY-3E/HIRAS-II are as follows:

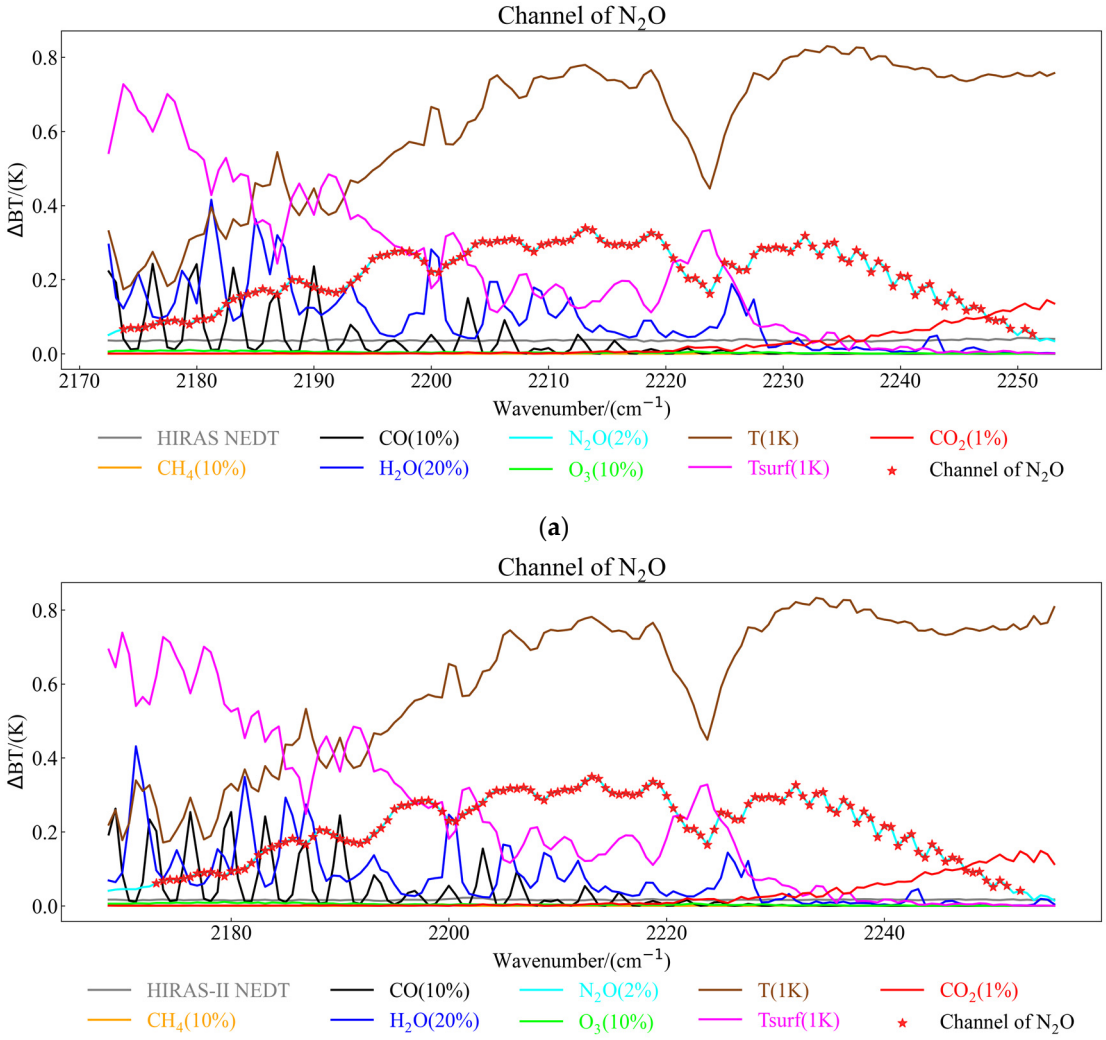


**Figure 13.** Results of short-wave infrared channel selection for $N_2O$: (**a**) FY-3D/HIRAS-I; (**b**) FY-3E/HIRAS-II.

From Tables 4–7, it can be observed that water vapor has the highest DFS and ER, followed by $O_3$. $N_2O$ and $CH_4$ come next, while CO and $CO_2$ have the lowest values. This observation is consistent with the sensitivity results discussed in Section 4.1, where higher sensitivity corresponds to greater information content. Overall, higher sensitivity leads to larger information capacity.

**Table 4.** DFS and ER of Atmospheric Gas Components for FY-3D/HIRAS-I (African Sea Region).

| Atmospheric Gas Components | DFS | ER |
|---|---|---|
| $H_2O$ | 5.24 | 16.82 |
| $O_3$ | 1.32 | 4.19 |
| $N_2O$ | 0.06 | 0.04 |
| $CH_4$ | 0.01 | 0.01 |
| $CO_2$ | 0.002 | 0.003 |
| CO | 0.001 | 0.001 |

**Table 5.** DFS and ER of Atmospheric Gas Components for FY-3E/HIRAS-II (African Sea Region).

| Atmospheric Gas Components | DFS | ER |
|---|---|---|
| $H_2O$ | 5.59 | 18.33 |
| $O_3$ | 1.59 | 5.07 |
| $N_2O$ | 0.04 | 0.03 |
| $CH_4$ | 0.01 | 0.01 |
| $CO_2$ | 0.01 | 0.01 |
| CO | 0.001 | 0.001 |

**Table 6.** DFS and ER of Atmospheric Gas Components for FY-3D/HIRAS-I (Chinese Yangtze River Delta terrestrial region).

| Atmospheric Gas Components | DFS | ER |
|---|---|---|
| $H_2O$ | 4.6 | 15.75 |
| $O_3$ | 1.45 | 4.86 |
| $N_2O$ | 0.12 | 0.1 |
| $CH_4$ | 0.07 | 0.06 |
| CO | 0.003 | 0.002 |
| $CO_2$ | 0.001 | 0.001 |

**Table 7.** DFS and ER of Atmospheric Gas Components for FY-3E/HIRAS-II (Chinese Yangtze River Delta terrestrial region).

| Atmospheric Gas Components | DFS | ER |
|---|---|---|
| $H_2O$ | 4.76 | 15.9 |
| $O_3$ | 1.81 | 6.37 |
| $N_2O$ | 0.31 | 0.27 |
| $CH_4$ | 0.14 | 0.1 |
| $CO_2$ | 0.01 | 0.01 |
| CO | 0.002 | 0.001 |

In theory, information content is an indicator of the performance of remote sensing systems. Greater information content indicates a stronger ability of the satellite observation system to retrieve target information. When comparing the information content of FY-3E/HIRAS-II with FY-3D/HIRAS-I, it can be concluded that HIRAS-II has better remote sensing performance and improved retrieval capabilities compared to HIRAS-I. The difference is most prominent for $H_2O$ and $O_3$, where HIRAS-II exhibits significantly greater information content than HIRAS-I. The improvement is also notable for $N_2O$ and $CH_4$, where HIRAS-II outperforms HIRAS-I. Analyzing the spectral coverage of the two hyperspectral instruments, HIRAS-II covers an additional long-wave range of 1135–1210 $cm^{-1}$ and a mid–short-wave range of 1750–2155 $cm^{-1}$ compared to HIRAS-I. HIRAS-II also includes the $O_3$ detection band of 2070–2130 $cm^{-1}$, which is missing in HIRAS-I. Therefore, HIRAS-II provides more comprehensive $O_3$ detection information and has a stronger ability to detect $O_3$ compared to HIRAS-I.

For FY-3D/HIRAS-I, the $H_2O$ ER (DFS) in the African maritime region is 1.07 (0.64) higher than that in the Yangtze River Delta region of China. On the other hand, the $O_3$ ER (DFS) in the Yangtze River Delta region of China is 0.67 (0.13) higher than that in the African maritime region. Similarly, the ER (DFS) for $N_2O$, $CH_4$, and other gases is also higher in the Yangtze River Delta region of China compared to the African region.

For FY-3E/HIRAS-II, the $H_2O$ ER (DFS) in the African maritime region is 2.43 (0.83) higher than that in the Yangtze River Delta region of China. In contrast, the $O_3$ ER (DFS) in the Yangtze River Delta region of China is 1.3 (0.22) higher than that in the African maritime region. The ER (DFS) for $N_2O$ in the Yangtze River Delta region is 0.27 (0.24) higher than

that in the African maritime region. Similarly, the ER (DFS) for $CH_4$ and other gases is also higher in the Yangtze River Delta region of China compared to the African region.

For the African marine region, the $H_2O$ ER (DFS) contained in FY-3E/HIRAS-II is 1.51 (0.35) higher than that in FY-3D/HIRAS-I. Similarly, the $O_3$ ER (DFS) in FY-3E/HIRAS-II is 0.88 (0.27) higher than that in FY-3D/HIRAS-I.

In the case of the Yangtze River Delta region of China, the $H_2O$ ER (DFS) contained in FY-3E/HIRAS-II is 0.15 (0.16) higher than that in FY-3D/HIRAS-I. Moreover, the $O_3$ ER (DFS) in FY-3E/HIRAS-II is 1.51 (0.36) higher than that in FY-3D/HIRAS-I, while the $N_2O$ ER (DFS) in FY-3E/HIRAS-II is 0.17 (0.19) higher and the $CH_4$ ER (DFS) is 0.07 (0.04) higher than that in FY-3D/HIRAS-I.

It is observed that the DFS and ER of each atmospheric component vary depending on the region, which is likely related to the concentration of atmospheric gases in each region. Generally, the information capacity of various atmospheric components in the Yangtze River Delta region of China is higher compared to the African marine region.

## 5. Discussion

Before the spectral information from satellite hyperspectral observations is used for remote sensing retrieval, it is crucial and necessary to perform sensitivity analysis, channel selection, and quantitative analysis of the information capacity of atmospheric detection data. In this experiment, we conducted sensitivity analysis, channel selection, and information capacity calculation for various atmospheric gas components based on the observed data from FY-3D/HIRAS-I and FY-3E/HIRAS-II satellites and the simulated results from the RTTOV fast radiative transfer model. During the analysis of the results, we found that:

When conducting sensitivity analysis of atmospheric gas components, we found that CO and $CO_2$ have the weakest sensitivity, while temperature, water vapor, ozone, methane, and nitrous oxide exhibit the strongest sensitivity. We discovered that FY-3E/HIRAS-II and FY-3D/HIRAS-I have different sensitivities to perturbations in various atmospheric gas components, and the sensitivities also vary across different experimental regions. Future comparative analysis will be conducted by selecting different experimental regions, such as during summer, and analyzing them at different experimental times.

In the experimental section of channel selection, we found that FY-3E/HIRAS-II has a higher number of channels selected for each component compared to FY-3D/HIRAS-I. Specifically, $CO_2$ and $N_2O$ channels can be selected for both long-wave and short-wave channels. It has been observed that the short-wave channels of both HIRAS-II and HIRAS-I are not very stable, and related works in the literature [14] have confirmed significant deviations in the short-wave range. However, despite the instability, the number of short-wave channels is still greater than the number of long-wave channels. In future studies, it will be necessary to increase the number of long-wave channels.

In the calculation results of DFS and ER, we found that CO and $CO_2$ have very low DFS and ER. In subsequent experiments, we will select the time and region with high concentrations of CO and $CO_2$. We will improve or use alternative methods for channel selection to continue calculating and analyzing the information capacity of CO and $CO_2$.

## 6. Conclusions

FY-3D/HIRAS-I is the first infrared hyperspectral instrument to be implemented on China's polar-orbiting meteorological satellites, while FY-3E/HIRAS-II is the first infrared hyperspectral instrument used on China's (and the world's) first sun-synchronous orbit civil operational meteorological satellite. It is important and meaningful to use these two instruments for atmospheric gas component retrieval. Therefore, we conducted sensitivity analysis, channel selection, and information capacity calculation after perturbing the gas components to quantitatively explore the retrieval capabilities of the instruments for atmospheric gas components. Preliminary research results indicate:

(1) FY-3D/HIRAS-I and FY-3E/HIRAS-II exhibit different sensitivities to atmospheric gas components. Temperature and water vapor show the most significant variations,

followed by $O_3$, $CH_4$, and $N_2O$, while CO and $CO_2$ exhibit the lowest sensitivities. Variations in temperature and water vapor are evident in different experimental regions, while the sensitivity differences for other gases are relatively small. Ozone's sensitive spectral bands are concentrated in the 1000–1125 $cm^{-1}$ and 2120–2125 $cm^{-1}$ bands, with FY-3E/HIRAS-II having an additional region of strong variation in the short-wave infrared band (2120–2125 $cm^{-1}$) compared to FY-3D/HIRAS-I. The sensitive spectral bands for $CH_4$ are concentrated in the 1250–1375 $cm^{-1}$ band; for $N_2O$, in the 1250–1300 $cm^{-1}$ and 2125–2250 $cm^{-1}$ bands; for CO, in the 2120–2140 $cm^{-1}$ band; and for $CO_2$, in the 740–750 $cm^{-1}$ and 2245–2255 $cm^{-1}$ bands;

(2) FY-3E/HIRAS-II has a higher number of gas channels selected compared to FY-3D/HIRAS-I, especially for $N_2O$, CO, and $CO_2$. Based on FY-3E/HIRAS-II data, there are 33 additional long-wave channels and 23 additional short-wave channels for $N_2O$ compared to FY-3D/HIRAS-I. Additionally, there are 34 more channels for CO and 53 more long-wave channels and 37 more short-wave channels for $CO_2$;

(3) FY-3E/HIRAS-II exhibits significantly greater information content than FY-3D/HIRAS-I, particularly for $H_2O$ and $O_3$. Upon analyzing the spectral coverage of the two hyperspectral instruments, it is evident that HIRAS-II surpasses HIRAS-I by covering an additional long-wave range of 1135–1210 $cm^{-1}$ and a mid–short-wave range of 1750–2155 $cm^{-1}$. In addition, HIRAS-II incorporates the $O_3$ detection band of 2070–2130 $cm^{-1}$, a feature absent in HIRAS-I. HIRAS-II also demonstrates notable improvement compared to HIRAS-I for $N_2O$ and $CH_4$. The information capacity of atmospheric gas components varies across different experimental regions. For the African marine region, the H2O ER (DFS) contained in FY-3E/HIRAS-II is 1.51 (0.35) higher than that in FY-3D/HIRAS-I and the O3 ER (DFS) in FY-3E/HIRAS-II is 0.88 (0.27) higher than that in FY-3D/HIRAS-I. In the case of the Yangtze River Delta region of China, the H2O ER (DFS) contained in FY-3E/HIRAS-II is 0.15 (0.16) higher than that in FY-3D/HIRAS-I. Moreover, the O3 ER (DFS) in FY-3E/HIRAS-II is 1.51 (0.36) higher than that in FY-3D/HIRAS-I, while the N2O ER (DFS) in FY-3E/HIRAS-II is 0.17 (0.19) higher and the CH4 ER (DFS) is 0.07 (0.04) higher than that in FY-3D/HIRAS-I.

In this experiment, we conducted a comparative analysis of the sensitivity, channel selection, and information capacity calculation for atmospheric gas components using the two instruments in different regions. We explored the infrared spectral coverage of atmospheric gas components by FY-3D/HIRAS-I and FY-3E/HIRAS-II, as well as the specific information contained for each gas component. Based on analysis of experimental results, it has been determined that FY-3E/HIRAS-II has more ozone bands compared to FY-3D/HIRAS-I, and it has also improved the detection accuracy of water vapor. Additionally, its capability of methane and other gases' inversion has also been enhanced. Our future research will focus on how to extract and effectively utilize this information, thereby providing a reference for improving the remote sensing retrieval capabilities of atmospheric gas components for both instruments. We will continue to explore the atmospheric inversion capabilities of the FY-3D and FY-3E satellite instruments and compare the advantages and disadvantages of different inversion methods, providing references and guidance for future research.

**Author Contributions:** Conceptualization, M.X., M.G. and C.Z.; methodology, M.X. and C.Z.; software, M.X.; validation, M.X. and C.Z.; formal analysis, M.X. and M.G.; investigation, M.X., P.H., H.L. and T.Y.; resources, M.X.; data curation, M.X. and M.G.; writing—original draft preparation, M.X., M.G. and Y.H.; writing—review and editing, M.X., C.Z., T.Y. and P.H.; visualization, M.G. and Y.H.; supervision, M.G. and Y.H.; project administration, M.G.; funding acquisition, M.G. All authors have read and agreed to the published version of the manuscript.

**Funding:** This research was funded by the Innovation Project of the Shanghai Institute of Technical Physics of the Chinese Academy of Sciences (No. CX-388).

**Data Availability Statement:** All the data generated or analyzed during this study are included in this article.

**Acknowledgments:** We would like to thank the NSMC (National Satellite Meteorological Center) for sharing FY3D/HIRAS and FY-3E/HIRAS-II data. We would also like to thank the ECMWF and WACCM for their openly accessible data. Meanwhile, we also would like to thank Mingjian Gu and Yong Hu of the Shanghai Institute of Technical Physics, Chinese Academy of Sciences, for equipment and technical guidance.

**Conflicts of Interest:** The authors declare no conflict of interest.

## References

1. Dong, C.-H.; Li, J.; Zhang, P. *The Principle and Application of Satellite Hyperspectral Infrared Atmospheric Remote Sensing*; Science Press: Beijing, China, 2013. (In Chinese)
2. Di, D.; Li, J.; Han, W.; Bai, W.; Wu, C.; Menzel, W.P. Enhancing the fast radiative transfer model for FengYun-4 GIIRS by using local training profiles. *J. Geophys. Res. Atmos.* **2018**, *123*, 12583–12596. [CrossRef]
3. Reeves, R.G. *Manual of Remote Sensing*; American Society of Photogrammetry: Falls Churen, VA, USA, 1975.
4. Rodgers, C.D. *Inverse Methods for Atmospheric Sounding: Theory and Practice*; World Scientific: Singapore, 2000; pp. 82–89.
5. Fourri'e, N.; Thépaut, J.N. Evaluation of the AIRS near-real-time channel selection for application to numerical weather prediction. *Q. J. R. Meteorol. Soc.* **2010**, *129*, 2425–2439. [CrossRef]
6. Collard, A.D. Selection of IASI channels for use in numerical weather prediction. *Q. J. R. Meteorol. Soc.* **2007**, *133*, 1977–1991. [CrossRef]
7. Ventress, L.; Dudhia, A. Improving the selection of IASI channels for use in numerical weather prediction. *Q. J. R. Meteorol. Soc.* **2014**, *140*, 2111–2118. [CrossRef]
8. Hou, W.; Wang, J.; Xu, X.; Jeffrey; Reid, S. An algorithm for hyperspectral remote sensing of aerosols: 2. Information content analysis for aerosol parameters and principal components of surface spectra. *J. Quant. Spectrosc. Radiat. Transf.* **2017**, *192*, 14–29. [CrossRef]
9. Crevoisier, C.; Clerbaux, C.; Guidard, V.; Phulpin, T.; Armante, R.; Barret, B.; Camy-Peyret, C.; Chaboureau, J.-P.; Coheur, P.-F.; Crépeau, L.; et al. Towards IASI-New Generation (IASI-NG): Impact of improved spectral resolution and radiometric noise on the retrieval of thermodynamic, chemistry and climate variables. *Atmos. Meas. Tech.* **2014**, *7*, 4367–4385. [CrossRef]
10. Luo, S.; Di, D.; Cui, L.-L. Study on FY-4A/GIIRS infrared spectrum detection capability based on information content. *Infrared Millim. Waves* **2019**, *38*, 765–776.
11. Zheng, F.-X.; Hou, W.-Z.; Li, Z.-Q. Optimal estimation retrieval for directional polarimetric camera onboard Chinese Gaofen-5 satellite: An analysis on multi-angle dependence and a posteriori error. *Acta Phys. Sin.* **2019**, *68*, 040701. [CrossRef]
12. Yang, Y.-H.; Yin, Q.; Shu, J. Channel selection of atmosphere vertical sounder (GIIRS) on board the FY-4A geostationary satellite. *J. Infrared Millim. Waves.* **2018**, *37*, 545–552.
13. Yang, T.; Zhang, C.; Zuo, F.; Hu, Y.; Gu, M. Uncertainty analysis of inter-calibration collocation based on FY-3E spaceborne infrared observations. *Infrared Laser Eng.* **2023**, *52*, 20220616.
14. Zhang, C.; Qi, C.; Yang, T.; Gu, M.; Zhang, P.; Lee, L.; Xie, M.; Hu, X. Evaluation of FY-3E/HIRAS-II Radiometric Calibration Accuracy Based on OMB Analysis. *Remote Sens.* **2022**, *14*, 3222. [CrossRef]
15. Yang, T.-H. *Tropospheric Wind Field Measurement Based on Infrared Hyperspectral Observations*; University of Chinese Academy of Sciences: Beijing, China, 2020.
16. Qi, C.-L.; Gu, M.-J.; Hu, X.-Q.; Wu, C. FY-3 Satellite infrared high spectral sounding technique and potential application. *Adv. Meteorol. Sci. Technol.* **2016**, *6*, 88–93.
17. Qi, C.L.; Zhou, F.; Wu, C.Q.; Hu, X.Q.; Gu, M.J. Spectral Calibration of Fengyun-3 high-spectral resolution infrared sounder. *Opt. Precis. Eng.* **2019**, *27*, 747–755.
18. Ren, J. Study on the Atmospheric Temperature and Humidity Profiles of Satellite Remote Sensing Based on One-Dimensional Variational Algorithm. Master's Thesis, Nanjing University of Information Science and Technology, Nanjing, China, 2018.
19. Xie, M.; Gu, M.; Hu, Y.; Huang, P.; Zhang, C.; Yang, T.; Yang, C. A Study on the Retrieval of Ozone Profiles Using FY-3D/HIRAS-I Infrared Hyperspectral Data. *Remote Sens.* **2023**, *15*, 1009. [CrossRef]
20. Zhang, C. *The Study for Retrieval of Temperature and Humidity Profiles and Trace Gas Profiles Based on Fengyun-3 Infrared Hyperspectral Data*; Shanghai Institute of Technical Physics, University of Chinese Academy of Sciences: Shanghai, China, 2023.
21. Hou, W.; Li, Z.; Wang, J.; Xu, X.; Goloub, P.; Qie, L. Improving Remote Sensing of Aerosol Microphysical Properties by Near-Infrared Polarimetric Measurements Over Vegetated Land: Information Content Analysis. *J. Geophys. Res. Atmos.* **2018**, *123*, 2215–2243. [CrossRef]
22. Pan, N.; Yu, F. Bias correction study on the satellite humidity retrievals through a one-dimensional variational method. *Chin. J. Geophys.* **2009**, *52*, 2973–2986.
23. Crevoisier, C. AIRS channel selection for $CO_2$ and other trace-gas retrievals. *Meteorol. Soc.* **2003**, *129*, 2719–2740. [CrossRef]

24. Rodgers, C.D. Information content and optimisation of high spectral resolution remote measurements. *Adv. Space Res.* **1996**, *21*, 136–147. [CrossRef]
25. Menke, W. *Geophysical Data Analysis: Discrete Inverse Theory*; Academic Press Inc.: New York, NY, USA, 1984.